Wave Breaking and Turbulence at a Tidal Inlet: Shoals, Currents, & Winds

Seth Zippel

A dissertation
submitted in partial fulfillment of the
requirements for the degree of

Master of Science in Civil Engineering

University of Washington

2014

Reading Committee:

James M. Thomson, Chair

Andrew T. Jessup

C. Chris Chickadel

Program Authorized to Offer Degree:
Civil and Environmental Engineering

University of Washington

Abstract

Wave Breaking and Turbulence at a Tidal Inlet: Shoals, Currents, & Winds

Seth Zippel

Chair of the Supervisory Committee:
Associate Professor James M. Thomson
Civil and Environmental Engineering

Field measurements of waves, currents, winds, and turbulence collected from surface drifters at New River Inlet (NC) are used to characterize wave breaking. Breaking regions are identified along drifter tracks by three separate metrics: decreases in wave energy flux, wave breaking counts from images, and elevated turbulent dissipation rates. Break points are used to evaluate the conventional depth breaking parameter, γ, and to develop a new breaking parameter, γ_u, which includes the effects of currents. The new breaking parameter has a more consistent critical value across all conditions because it successfully accounts for enhanced breaking with opposing currents and depressed breaking with following currents. In addition, turbulent dissipation rates correlate better with γ_u than with γ when currents are present. A TKE (turbulent kinetic energy) budget is discussed where the change in TKE is due to the balance between wave breaking and turbulent dissipation. Net energy input and change in TKE are well-matched but the magnitudes are offset. This suggests that other terms in the balance such as transport of TKE, generation of MKE (mean kinetic energy), and bubble dynamics are important to the overall energetics of the inlet. Offshore of the inlet, away from the shoals and currents, whitecaps are common, and the turbulent dissipation rates are correlated with windspeed, consistent with previous studies.

TABLE OF CONTENTS

Page

List of Figures ii

Chapter 1: Introduction 1
1.1 Describing a Wave Field 2
1.2 Linear Dispersion 4
1.3 Depth Shoaling 4
1.4 Depth Limited Breaking 5
1.5 Wave-Current Interactions 7
1.6 Wave Breaking Turbulence 8
1.7 Wind and Whitecaps 10

Chapter 2: Methods 11
2.1 A New Breaking Parameter: γ_u 11
2.2 Observations 12

Chapter 3: Results 21
3.1 Selected Tracks (8 tracks) 21
3.2 Full Data Set (500 tracks) 26
3.3 Fixed Array 30

Chapter 4: Discussion and Interpretation 32
4.1 Breaking Parameters 32
4.2 Turbulence and Breaking 33
4.3 Wind Effects 36

Chapter 5: Conclusion 39

Appendix A: Turbulent Structure Function Sensitivities 44

Appendix B: Ray Tracing 56

LIST OF FIGURES

Figure Number Page

1.1 Waves shoal from both depths and currents effects. When currents oppose waves (green profile) waves shoal in deeper water than from depth effects alone. On flood tides waves travel farther shoreward before breaking. 9

2.1 **(a)** New River Inlet, NC during low tide. Wave breaking can be seen on the shallow shoals on the sides of the inlet as well as across the channel mouths. Photo: Gordon Farquharson. **(b)** Bathymetry contours (1 m) and SWIFT drifter tracks for which onboard images were processed. Bathymetry data was collected on May 2nd, 2012 by the Army Corps FRF LARC survey system. The map is rotated into a cross-shore, along-shore coordinate system; a 59 degree rotation from true north. Ebb tracks are shown in light green, floods tracks are shown in magenta. Black dots denote the center of five minute average positions. Colored circles show locations of wave breaking. 13

2.2 Cartoon schematic of a SWIFT drifter shows the buoy's dimensions, instrument locations, and waterline. 14

2.3 Comparison of SWIFT 5 minute spectra with 1 hour spectra from pressure data of the collocated array on May 2nd. The comparison is made in wavenumber space to avoid confusion between the absolute frequency ω, and intrinsic frequency σ 16

2.4 Two examples of structure function fits to $r^{\frac{2}{3}}$ with the resulting dissipation rate profiles are shown above. **(a)** and **(b)** show linear fits between the structure function and $r^{\frac{2}{3}}$. Separation distances $(r - \Delta r)$ are used to correct for platform motion. The slope of the best fit line, $A(z)$ is used to estimate dissipation rates $\epsilon(z)$ in **(c)** and **(d)**. Examples taken from the SWIFT methods paper (Thomson et al., 2012). 18

2.5 An example GoPro image with a breaking wave. The discoloration of the water surface was due to a rhodamine dye release earlier that day. 20

3.1 Example ebb SWIFT drift on May 20th, 2012. The SWIFT was deployed inside the inlet (left) and drifted offshore (right) as time progressed. Panel **(a)** shows wave energy flux. Panel **(b)** shows breaking count from onboard images. Panel **(c)** shows turbulent dissipation rate beneath the waves. Panel **(d)** shows three non-dimensional parameters. Panel **(e)** shows the bathymetry and the measurement tidal currents (scaled arrows). 23

3.2 Example flood SWIFT drift on May 13th, 2012. The SWIFT was deployed offshore (right) and drifted into the river inlet (left). Panel **(a)** shows wave energy flux. Panel **(b)** shows breaking count from onboard images. Panel **(c)** shows turbulent dissipation rate beneath the waves. Panel **(d)** shows three non-dimensional parameters. Panel **(e)** shows the bathymetry and the measurement tidal currents (scaled arrows). 24

3.3 Values of γ and γ_u at the break point. Green x's represent data collected on ebb tides when waves oppose currents. Magenta x's represent data collected on flood tides when waves follow currents. The sign of $\cos\theta$ was used instead of the value when calculating γ_u (Equation 2.2) because wave directions were mostly collinear with the currents. The range of γ is larger than γ_u. (See Table 3.1 for actual values.) 25

3.4 Turbulent dissipation rate profiles averaged together in two categories, above critical and below critical values , each for γ (black) and γ_u (red). A critical value of 0.35 was used, although results shown in Table 3.2 show low sensitivity to variations of the critical value. Profiles are conditioned for $|U| > 0.5$ m/s because for low currents $\gamma \approx \gamma_u$. Profiles with wind speeds greater than 5 m/s are also excluded to reduce whitecap effects. Turbulent dissipation rate profiles were normalized by available wave energy flux because the range of offshore waves conditions varied during the experiment, and larger waves sampled on flood would otherwise bias flood dissipation rates high. 330 profiles were averaged together for the mean subcritical profile, and 100 for the mean supercritical profile. Standard errors for the profiles ranged between 15% and 20%. 28

3.5 Depth averaged dissipation rates normalized by available wave energy flux versus the breaking parameters γ (black) and γ_u (red). The area of the circle represents the number of samples included in the bin average, from a total of 330 samples. The dashed red line represents the critical value of γ_u. 29

3.6 Histograms of γ **(a)** and γ_u **(b)** from fixed array pressure sensors and ADVs **(c)** located near the example SWIFT flood and ebb tracks in space and time. The data from the fixed sensors were averaged over 512s intervals. The full array of sensors is shown, but only data from instruments close to the SWIFT tracks shown in Figures 3.1 and 3.2 is used to make the histograms. 31

4.1 Select terms from the TKE budget for the example ebb SWIFT track shown in Figure 3.1. Spacing of points along the x-axis is not uniform, as the drift speed changed over the deployment. The transparent red box indicates the breakpoint. 35

4.2 Depth averaged dissipation rates (black line) and wind energy input (blue line) versus along track distance. These values are offshore, in deep water ($\gamma < 0.1$) where a SWIFT was left to drift with the wind and waves. S_{wind} is calculated as formulated in Equation 1.8, using a phase speed estimated as the weighted average speed of wave period greater than 6 seconds. 37

4.3 Turbulent dissipation rate profiles as a function of depth bin averaged by wind speed. Profiles are thresholded for depth and current limited wave breaking by using low values of γ. Dissipation rates increase with increased wind, with the most dramatic increases in the top 30cm os the water column. 38

A.1 Sample time series of the top five velocity bins as measured from the Nortek HR Aquadopp on board a SWIFT drifter. Only 5 of the 16 bins are shown because of space limitations. Missing values in the time series are due to quality control processing based on beam correlations and return intensity as described in Thomson et al. (2012). Data is processed in 5 minute bursts, the first 1024 samples are used for each 5 minute burst. 45

A.2 Example dissipation profile created such that the area under the curve is equivalent to a given $\dot{E}$. The values presented here are larger than ones typically seen in situ. 48

A.3 Structure Function values calculated from an $r^{\frac{2}{3}}$ dependance 48

A.4 Cross Covariance Sequence at zero time lag between spatial lags down from the bin nearest the surface 50

A.5 Model and Given variance for each depth bin 51

A.6 10000 Monte Carlo Simulations of dissipation profiles build from a WN model. Realizations are shown in grey, the average is shown with standard deviations in black, and the input profile is shown in blue. 51

A.7 Ratio of synthetic $\dot{E}$ to the prescribed $\dot{E}$ increases with added noise. 52

A.8 A step-function type energy input (bottom) with a sample velocity profile (top). 53

A.9 Ratio of 'measured' E to the given E decreases with the duration of the turbulent event until the noise floor is reached at Percent Breaking $\approx 3\%$ . . 54

B.1 Wave Rays bend toward lines of constant bathymetry. Headlands focus wave rays as seen above. 57

B.2 Wave Rays bending over bathymetry with an offshore period of 5 seconds. . . 58

B.3 Wave Rays bending over bathymetry with an offshore period of 7 seconds. . . 59

B.4 Wave Rays bending over bathymetry with an offshore period of 10 seconds. . 60

B.5 Wave rays refract due to a gradient in currents. When currents oppose the wave directions, the wave rays bend to face the currents. Some wave rays are trapped in the opposing jet. 61

ACKNOWLEDGMENTS

Funding for this project was provided by the Office of Naval Research. Thanks to the field engineers J. Talbert and A. de Klerk for their help developing the SWIFT drifters and collecting the field data. Thanks to C. Bassett, R. Carini, J.P. Rinehimer, and M. Schwendeman for helpful conversations. Thanks to B. Raubenheimer and S. Elgar for sharing data and providing feedback on the manuscript. SWIFT data can be found at http://www.apl.washington.edu/project/project.php?id=darla

DEDICATION

To my family:

Your love and kindness hold me up when I would have fallen. Thank you for believing in me.

Chapter 1

INTRODUCTION

Breaking waves drive sediment transport and nearshore circulation and are thus important to the evolution of tidal inlets. To first order, inlet morphology is dependent on the ratio of incident wave energy to tidal energy (Hayes, 1980). Even in tidally dominated systems, large breaking waves during storms can move sediment offshore (Gallagher et al., 1998) and smaller scale nearshore morphological features have been shown to change based on wave conditions on short (order one week) timescales (Wright and Short, 1984; Lippmann and Holman, 1990). Wave induced currents can be important to the overall circulation of an inlet. On a uniform beach, gradients in wave radiation stresses drive alongshore currents (Longuet-Higgins, 1970). These wave driven currents can push flow toward an inlet along the coast even during ebb tide (Demirbilek and Vincent, 2008). In addition, surf-zone (wave breaking) effects can trap water exiting on ebb tides in the nearshore (Clark et al., 2014). Characterization of wave breaking can help explain patterns of circulation and sediment transport at inlets.

When a wave breaks, energy is transferred into turbulent kinetic energy (TKE), mean kinetic energy (MKE), bubbles, and sound (Longuet-Higgins, 1970; Battjes and Janssen, 1978; Lamarre and Melville, 1991). The breaking process and subsequent turbulence are key drivers of mixing and transport near the shore, including the suspension and dispersion of pollutants, microbes, and sediment (Hoefl and Elgar, 2003). Wave breaking can also be a hazard to vessels and marine structures. This paper presents observations and a modified breaking parameter to diagnose the occurrence and strength of breaking at a tidal inlet, where currents can have significant effects on wave breaking.

The three mechanisms controlling wave breaking in a tidal inlet are depths, currents, and winds. Waves shoal over bathymetry as they approach the inlet; as depth decreases, the wave group velocity decreases and the wave height grows via conservation of wave

action (Mei, 1989). On ebb tides, opposing currents further slow wave progress over ground, causing an additional increase in wave height via conservation of wave action. The combined effects of depth shoaling and opposing currents cause regions of enhanced wave breaking and turbulence, known as ebb shoals (Woodroffe, 2002). On flood tides, following currents increase wave speed over ground and thereby decrease wave heights (via conservation of wave action). Therefore waves on flood tides progress farther into shallower water before breaking, as the wave-current interaction counteracts depth shoaling in flood cases. Winds, although primarily considered for deep water breaking cases (i.e., whitecaps), are another mechanism for wave breaking and turbulence at an inlet. Wind stress at the water surface creates short, steep waves that break and enhance near surface turbulence (Melville, 1996).

Previous work is reviewed in §1. Methods are presented and described in §2, including a new breaking parameter, γ_u, the study site, the instrument deployments, and the data processing. Example drifter data, and the evaluation of γ_u are shown in §3. In §4 an energy budget and wind effects are discussed. Conclusions are stated in §5.

1.1 Describing a Wave Field

Waves are often described mathematically as monochromatic (single frequency) sinusoidal waves, but any casual ocean observer can attest that the ocean surface looks more complex. These irregular ocean surfaces can still be described by sinusoidal functions; using Fourier analysis to describe the surface as the summation of a cosine terms each with their own amplitude, frequency, and phase:

$$\eta(t) = \sum_n A_n \cos(\omega_n t + \phi_n) \tag{1.1}$$

Where $\eta(t)$ is the sea surface displacement from mean sea level as a function of time, t, and A_n, ω_n, and ϕ_n are the amplitude, frequency, and phase for the for the n^{th} component of the series. In this way, a summation of monochromatic waves with amplitude A, frequency ω, and phase ϕ_n, can describe an irregular sea surface. It is common to show this description of a sea surface as a power spectrum (a.k.a energy spectrum), where the square of sea surface height components, $E_n = A_n^2$ is plotted against their respective frequencies ω_n.

Conventionally the subscripts are dropped so that E is a function of ω, $E(\omega)$. This gives a statistical description of the irregular, or random sea surface. A complete description of a wave field also includes the wave direction, θ, per frequency component, such that the power spectrum is a function of both ω, and θ (i.e. $E(\omega, \theta)$.

Although the power spectrum provides a more detailed description of the wave field, it is common to use bulk parameters for ease of computation. Significant wave height, mathematically defined as $4\sqrt{\text{Var}(\eta)}$ (where Var is the variance) is the most common bulk parameter for wave height. Statistical properties of a power spectrum require the integrated spectrum, $\int E(\omega)d\omega$, to equal the variance of the sea surface height, $\text{Var}(\eta)$, such that significant wave height is often defined $H_s = 4\sqrt{\int E(\omega)d\omega}$. Defined as the the mean of the largest third of waves in the wave field, significant wave height is used because its mathematical definition matches historic records of visually observed wave heights made by trained mariners (Munk, 1944). Bulk parameters for frequency can differ. The two most common bulk frequency parameters are the peak wave frequency, ω_p, and the centroid frequency ω_c, defined as the weighted average of the frequencies $\frac{\int \omega E(\omega)d\omega}{\int E(\omega)d\omega}$. Bulk wave directions are often taken as the direction at the peak frequency θ_p, or the centroid direction Bulk wave directions are often taken as the direction at the peak frequency θ_p, or the centroid direction $\theta_c = \frac{\int \theta(\omega)E(\omega)d\omega}{\int E(\omega)d\omega}$.

Waves are often grouped into different frequency regimes. Low frequencies, typically periods $30s > T_p > 10s$, or frequencies $0.033 < f < 0.1$Hz, are called swell, and are often well approximated as a single monochromatic wave. Waves with higher frequencies generated by local wind are called 'sea'. Wind waves, or 'seas', are typically steeper than swells and thus have more contributing frequency components, ω_n. Frequencies higher than wind seas are often referred to as the equilibrium range, which is discussed in §1.7. Wave frequencies below the swell range are not discussed in this paper.

The energy in a monochromatic Airy wave can be shown analytically to be $E = \frac{1}{8}\rho g H^2$. Although the power spectrum is often notated $E(\omega)$ it should be noted that the constants are often dropped so the units of the power spectrum are $\frac{\text{m}^2}{\text{Hz}}$.

1.2 Linear Dispersion

The dispersion relation is central to understanding wave mechanics. The linear dispersion is:

$$\omega = \sqrt{gk \tanh kd} \tag{1.2}$$

where ω is the absolute frequency of the wave, k is the wave number defined as $k = \frac{2\pi}{L}$ where L is the wavelength, g is the acceleration due to gravity, tanh is the hyperbolic tangent function, and d is the water depth. The dispersion relation is often rewritten in terms of phase speed $C = \frac{\omega}{k}$, so that $C = \frac{g}{\omega} \tanh kd$. In this form we see that long (low frequency) waves travel faster than short waves. In shallow water this difference is small as $\tanh kd \approx kd$, and the wave speed $C = \sqrt{gd}$ is only a function of depth. This is essential in understanding wave shoaling and refraction nearshore described in the following sections.

1.3 Depth Shoaling

The flux of wave energy, which propagates with the group velocity C_g, is conserved rather than the wave energy E. The conservative energy equation, called the wave action balance, describes the process of wave shoaling:

$$\frac{\partial}{\partial t}\left(\frac{E}{\omega}\right) + \nabla \cdot \left(\frac{E}{\omega}\right) C_g = 0, \tag{1.3}$$

where $\frac{E}{\omega} = \frac{\rho g H_s^2}{8\omega}$ is wave action assuming a monochromatic wave, t is time, C_g is group velocity, ∇ denotes a horizontal spatial derivative, and H_s is significant wave height. Here, the frequency integrated wave action balance is used, where $\frac{E}{\omega}$ is replaced with E. This describes the total wave energy in a natural wave spectrum $E(\omega)$, however it obscures the known nonlinearities that transfer energy between spectral components during shoaling (Freilich et al., 1990; Elgar et al., 1995) and breaking (Herbers et al., 2000).

Wave refraction can be understood through the dispersion relation; waves travel faster in deep water and slower in shallow water (Equation 1.2). As a wave crest moves over bathymetry, the difference in wave speed across the crest will curve the wave towards lines

of constant bathymetry as the faster, deeper section of the wave crest outruns the slower, shallower section. Wave energy is focused in locations where wave rays (lines normal to the wave crests) converge. The opposite is also true; as wave rays diverge, wave energy is spread out. The horizontal divergence term in the wave action balance accounts for this spreading of energy between wave rays. For relatively straight coasts, a 1-D case can be reduced to $\frac{d}{dx}(EC_g) = 0$, where the local changes $\frac{\partial}{\partial t}$ are assumed small and all changes are in a cross-shore direction x. For more discussion on wave refraction, see Appendix B.

In shallow water the group velocity is simply $C_g = \sqrt{gd}$, and thus as the group velocity decreases with water depth d, the wave energy, $E \sim H^2$, must increase. Because deep water waves are dispersive, the change in wave height at a particular depth depends on the offshore C_g, which is a function of frequency. Therefore an offshore wave at low frequency will experience a larger height increase in shallow water than a high frequency wave (i.e., shoaling is a more significant effect for long waves).

Wave lengths decrease during the shoaling process. This is seen through the dispersion relation and conservation of absolute frequency. In shallow water, the absolute frequency is approximated: $\omega = k\sqrt{gd}$ (see Equation 1.2). Because absolute frequency ω is constant, as the depth, d, decreases the wavenumber k must increase (or the wavelength decreases). Therefore the wave steepness, kH_s, is increased in shoaling both by larger wave height, H_s, as seen through the wave action balance and by higher wavenumber, k, (shorter wavelengths) through the dispersion relation.

1.4 Depth Limited Breaking

Steepening from shoaling cannot continue indefinitely because waves break when they reach a critical steepness. Shoaling and depth limited breaking have often been diagnosed through the simple non-dimensional parameter $\gamma = \frac{H_s}{d}$ (Iverson, 1952; Bowen et al., 1968; Méhauté et al., 1968; Longuet-Higgins, 1970; Thornton and Guza, 1982, 1983). This followed from the work of Miche (Miche, 1954) who posed a steepness limitation on breaking $Hk = 0.88 \tanh(\frac{\gamma}{0.88}kd)$ which reduces to $\gamma = \frac{H_s}{d}$ in shallow water. Critical values of γ have been shown to vary between 0.3 and 0.8 (Demirbilek and Vincent, 2008). It should be noted that this range of critical values variable between beaches, and is not expected to vary between

0.3 and 0.8 for a specific beach. Early studies of γ posed the parameter as a function of both beach slope and offshore wave height. Further work on γ has shown the dependence on offshore wave slope to be small (Sallenger Jr. and Holman, 1985; Raubenheimer et al., 1996). Raubenheimer et al. (1996) found that the parameter could be expressed as a function of beach slope and depth relative to wavelength, $\gamma = C_0 + C_1 \frac{\beta}{kd}$. For shallow sloping beaches where $\beta \approx 0$ this reduces to a constant value, consistent with previous results. Similarly, for deep water cases where kd is large, γ approaches a constant value such that the formulation remains consistent with Miche (1954). When γ reaches a critical value, γ_{brk}, the wave will break and its height will decrease such that $\gamma \leq \gamma_{brk}$. The surf zone is considered fully saturated when $\gamma = \gamma_{brk}$ from the initial break point until the wave bore reaches shore. In an idealized, saturated, surf zone, every wave has a foamy turbulent crest and wave height constant to the relative depth (i.e. $\frac{H_s}{d} = \gamma_{brk}$).

Upon breaking, wave action is no longer conserved because wave energy is lost to turbulence, mean currents, bubbles, and sound. A wave energy dissipation (loss) rate ϵ_{brk} is introduced to the wave action balance, such that

$$\frac{d}{dx}(EC_g) = \rho \int \epsilon_{brk} dz, \tag{1.4}$$

where the wave energy dissipation rate ϵ_{brk} is volumetric (units are $\mathrm{m}^2\ \mathrm{s}^{-3}$) to match the convention for the turbulent kinetic energy (TKE) dissipation rate, though these are not assumed, a priori, to be equal.

Previous studies have characterized wave energy dissipation rate ϵ_{brk} based on wave parameters. Battjes and Janssen (1978) modeled the wave bore formed after breaking as a hydraulic jump and described the energy loss as the difference in hydraulic head on either side of the bore. The resulting equation is:

$$\epsilon = \frac{1}{4} \rho g H_{max}^2 Q_b f_p \tag{1.5}$$

where Q_b is the fraction of breaking waves observed, and f_p is the peak frequency. The wave height H_{max} is determined from Miche's steepness criterion, $\gamma_{brk} = \frac{H}{d}$, as described in the previous section. The term $Q_b f_p$, the breaking fraction multiplied by the frequency of

breaking waves, is the number of breaking wave crests compared to the number of expected crests based on the wave frequency. Battjes and Janssen (1978) prescribed Q_b assuming a Rayleigh distribution of wave heights in the surf zone. All of the waves in the distribution above H_{max} are assumed to be breaking, and the fraction of breaking Q_b is then the area of the distribution above H_{max}.

Thornton and Guza (1983) proposed a similar dissipation model, but used a Rayleigh distribution of breaking waves. This method allows for a distribution of broken waves centered around a maximum wave height, as opposed the strict cut-off used by Battjes and Janssen (1978). In other words, rather than requiring all waves above a critical height to break, the Thornton and Guza (1983) model prescribes a statistical distribution breaking waves heights. Both dissipation models are in use today (e.g., Chawla and Kirby (2002)).

1.5 Wave-Current Interactions

The wave action balance can be modified to incorporate currents, such that (Kirby, 1984)

$$\frac{\partial}{\partial t}E + \nabla \cdot E(C_g + U) = \rho \int \epsilon_{brk} dz. \tag{1.6}$$

Waves shoal against an opposing current due to a change in wave speed over ground $C_g + U$, similar to how waves shoal in shallow water as the group velocity C_g decreases due to depth. The linear dispersion relation also must be amended to include the presence of currents, such that

$$\omega = \sigma + \vec{u} \cdot \vec{k}, \tag{1.7}$$

where $\sigma = \sqrt{gk \tanh(kd)}$ is the intrinsic (stationary to water) frequency of the wave, ω is the absolute (stationary to ground) frequency of the wave, and the vector dot product $\vec{u} \cdot \vec{k}$ is the frequency adjustment due to currents where the vectors indicate the direction of the waves, $\vec{k}$, and the currents, $\vec{u}$. The term $\vec{u} \cdot \vec{k}$, which arises directly from a change of inertial reference frame, is often misnamed a Doppler shift (Gerkema et al., 2012). This can be misleading when using the popular analogy of a car driving by a stationary observer. In the analogy, the speed of sound remains constant while the frequency and wavelength of

the sound wave are adjusted due to the motion of the source. In the case of wave current interaction, two observers are moving relative to each other, thus two possible observed frequencies arise (intrinsic and absolute), and two possible observed speeds (over water, over ground). The distinction between the two cases is subtle but necessary, as absolute frequency is conserved in the wave/current case (but not in the sound case, which is why the pitch changes as a the car passes in the analogy).

For large currents relative to the wave speed, the modified dispersion relationship results in imaginary wave numbers. This phenomena is known as wave blocking, and occurs when the Froude number, defined as $Fr = \frac{u}{c}$ (where c is the wave phase speed) is -0.5 (Mei, 1989). For deep water waves Fr is frequency dependent, and high frequencies can be blocked as lower frequencies show little wave-current effect ($\vec{u} \cdot \vec{k}$ is small for $k << 1$). Shallow waves have the same wave speed ($C = \sqrt{gd}$) relative to water and do not experience the same frequency dependence. Since the wave action balance holds true along ray paths which become caustic (i.e. ray-paths cross and wave energy becomes undefined) in the wave blocking case, use of the equation to study wave-current interaction is not well posed.

Still, Equation 1.6 is useful to study the effects of currents. Prior to blocking, the effect of $C_g + U$ is to change wave heights. As before, wave breaking will occur if the wave is critically steep. Chawla and Kirby (2002) showed that down stream (up wave) of the blocking point, high frequencies are increased in amplitude and steepness. Energy weighted average frequencies were reduced upstream (down wave) of the blocking point in wave-current cases due to the breaking of higher frequency wave components.

1.6 Wave Breaking Turbulence

The energy lost from waves during breaking is thought to become turbulence, though a direct 1:1 accounting of the energy has yet to be shown in the surf zone. Turbulence transfers energy to smaller and smaller scales until the energy is dissipated by viscosity at the smallest scales (the Kolmogorov micro scales) where it is lost to heat (Kolmogorov, 1941). The transfer from large scales to the dissipative scales requires time and space, and therefore TKE is not always dissipated locally as mean currents advect it away from a source.

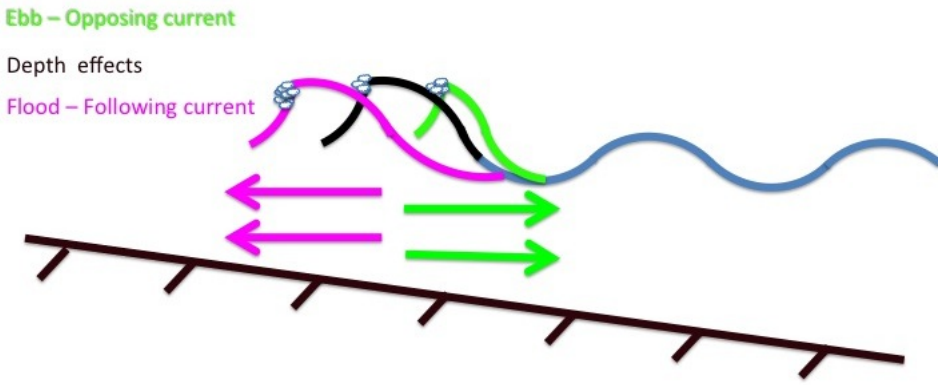

Figure 1.1: Waves shoal from both depths and currents effects. When currents oppose waves (green profile) waves shoal in deeper water than from depth effects alone. On flood tides waves travel farther shoreward before breaking.

Previous studies have shown a correlation between energy lost in wave breaking and turbulent dissipation rates, but the two often differ by a factor of 100 (Feddersen, 2012; Thomson, 2012). Feddersen (2012) examined multiple scalings in the surf zone comparing TKE (turbulent kinetic energy) to change in wave energy flux. The differences in magnitude are attributed to measurements taken below the areas of highest dissipation, where TKE is expected to stay near the surface. Thomson (2012) measured turbulent dissipation rates in the top 60cm of the water column in the surf zone, but still observed a large difference in magnitude between wave energy flux gradient and dissipation rate. Here the discrepancy was attributed to intermittence, TKE outside the measured control volume (which did not extend to the full water column), wave reflections, MKE (mean kinetic energy), and bubbles (buoyancy work). More information about the effect intermittence on measured TKE dissipation rates is available in Appendix A. Lamarre and Melville (1991) estimated up to 30%-50% of the wave breaking energy loss in deep water waves can be attributed to bubble formation and is a function of wavelength and void fraction (the ratio of volume of air to volume of water), but this alone cannot explain the local imbalance between the energy lost in wave breaking and TKE energy dissipation.

1.7 Wind and Whitecaps

Wind transfers momentum into the ocean surface, creating short waves. Strong winds cause these waves to break (and form whitecaps). Over short distances and small time scales the balance between energy input into waves from wind, S_w, and energy loss from wave breaking, $\int \epsilon_{brk} dz$, are approximately equal. The frequency bands over which this holds true are called the equilibrium range and follows the relationship $E(\sigma) \sim \sigma^{-4}$ (Phillips, 1985). The input of energy from the wind into the waves is slightly larger than the whitecapping breaking energy loss, so that over enough time and distance (fetch) waves can grow. The wind source term can be estimated as:

$$\int S_w d\sigma = c_e \tau \tag{1.8}$$

where c_e is an effective transfer velocity (Gemmrich et al., 1994) often taken as $\frac{c_p}{2}$, (where c_p is a the wave phase speed) and wind stress τ scales as $\tau = \rho_a c_d u_{10}^2$ with air density ρ_a and drag coefficient c_d often taken to be 1.3 and $1.5 * 10^{-3}$ respectively. This balance has been validated in the open ocean by Thomson et al. (2013) and is expected to hold wherever wind forcing is the dominant dynamic, including offshore of tidal inlets.

Chapter 2

METHODS

2.1 A New Breaking Parameter: γ_u

The depth limited breaking parameter γ has been shown to work well for beach settings, but the critical value of γ (where breaking begins) is modulated by currents and is less adequate at prescribing a consistent breaking point at tidal inlets. As seen in Equation 1.6, currents modulate the shoaling of waves. Therefore, on ebb tides, waves break at small values of γ because the shoaling due to currents adds to the shoaling from depth. The converse is true on flood tides, and breaking occurs at larger values of γ. A new parameter, γ_u is defined in order to better prescribe regions of breaking in the presence of depth and currents.

With the conventional γ rewritten in terms of shallow-water wave group speed

$$\gamma = \frac{H_s}{d} = \frac{H_s g}{C_g^2}, \tag{2.1}$$

the new parameter γ_u is defined by simply adjusting the speed term with a signed current speed U,

$$\gamma_u = \frac{H_s g}{(C_g + U\cos\theta)^2}. \tag{2.2}$$

Here, θ is the angle between the waves and the currents. When waves and currents oppose each other, $U\cos\theta$ is negative and γ_u increases. Conversely, when waves follow currents, $U\cos\theta$ is positive and γ_u decreases. In this way the critical value of γ_u stays constant between ebb and flood cases, while the critical value γ is low on ebb tides and high on flood tides. Note that for $U = 0$ or $\cos\theta = 0$ the new parameter reduces to the solely depth limited parameter, i.e. $\gamma_u(U = 0) = \gamma$.

2.2 Observations

The study site, New River Inlet, was chosen as part of a large collaborative study on inlets. New River Inlet is located south of the Outer Banks near Marine Corps Base Camp Lejeune in North Carolina (USA). It is frequently dredged, and is bisected by the Inter Coastal Waterway. In the inlet, a northern channel closer to Onslo Beach was historically dredged, but has been left to fill in. A southern channel closer to North Topsail Island is now maintained for marine traffic. Both channels are visible by aerial photograph (Figure 2.1a).

High and low tide are in phase with max flood and ebb currents (i.e., progressive tide). Tide variations from mean sea level are on the order of $\pm$0.5m for neap tides and $\pm$1m for spring tides. Currents were consistently larger than 1 m/s, and measured as high as 1.5 m/s. Offshore wave heights during the experiment were typically $H_s \leq 1$ m with peak periods in the 7-9 second range. The beach faces southeast (approximately 140 degrees true). The freshwater input from the river is small; the flows are primarily tidal.

SWIFT drifters, which are Lagrangian wave buoys specializing in near surface measurements (Thomson, 2012), were deployed at the inlet between April 26th and May 21st, 2012. The SWIFTs measure wind (using an Airmar PB200); location, drift speed, and waves (using a Qstarz BT-Q1000eX GPS); turbulent dissipation rate (using a Nortek 2MHz Aquadopp HR); take images (using a GoPro Hero); and have local tracking (using Garmin Astro collars).

SWIFT drifters were designed to be light and easily deployable by a single operator. The SWIFT has 1.25m of draft and a 0.9m mast, adding for a total height of 2.15m (2.2). The SWIFT is widest at the flotation foam, with a diameter of 0.3m. The flotation gives the SWIFT 2.7Kg of buoyancy which is counteracted by 2.6Kg of lead ballast located in the bottom heave plate. The SWIFT bobs at a natural frequency of approximately 1.3s (Thomson et al., 2012).

SWIFTs were deployed on drifts lasting 1-4 hours each, and were deployed for multiple drifts per day. Daily operations with up to six SWIFTs running at a time lasted anywhere from 3 to 12 hours. Occasionally a SWIFT would run aground and have to be reset; this

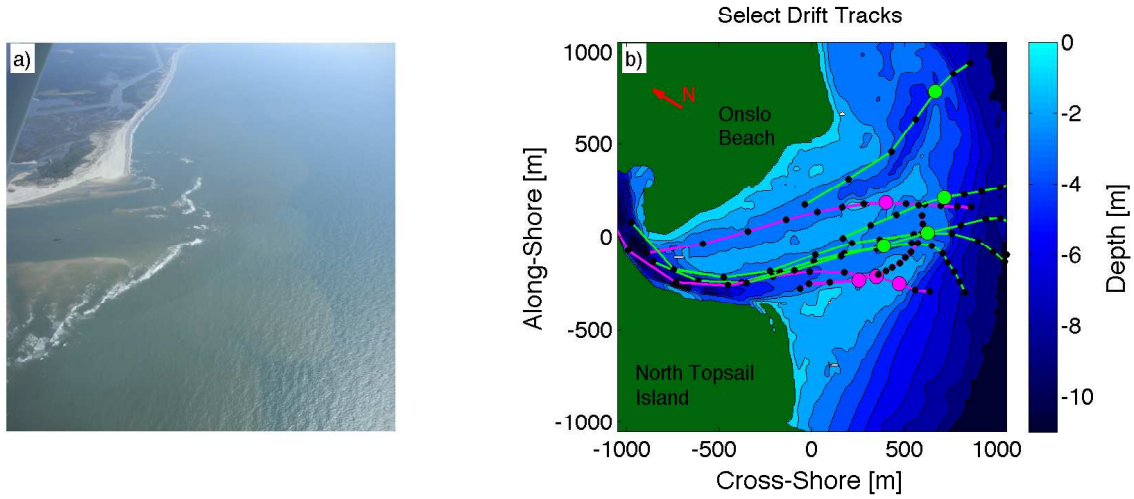

Figure 2.1: **(a)** New River Inlet, NC during low tide. Wave breaking can be seen on the shallow shoals on the sides of the inlet as well as across the channel mouths. Photo: Gordon Farquharson. **(b)** Bathymetry contours (1 m) and SWIFT drifter tracks for which onboard images were processed. Bathymetry data was collected on May 2nd, 2012 by the Army Corps FRF LARC survey system. The map is rotated into a cross-shore, along-shore coordinate system; a 59 degree rotation from true north. Ebb tracks are shown in light green, floods tracks are shown in magenta. Black dots denote the center of five minute average positions. Colored circles show locations of wave breaking.

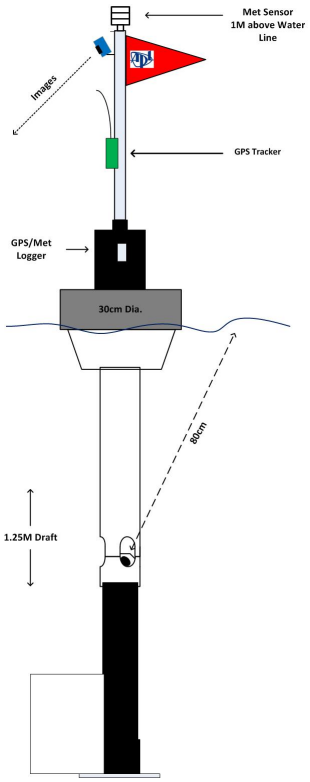

Figure 2.2: Cartoon schematic of a SWIFT drifter shows the buoy's dimensions, instrument locations, and waterline.

data is excluded from subsequent analysis.

2.2.1 Wave spectra

SWIFT measurements were processed in 5 minute bursts. SWIFT wave spectra were made from horizontal velocities sampled at 5Hz following the method described in Herbers et al. (2012). Spectra from the linearly detrended horizontal velocity components u and v were made by averaging 16 windows of Fast Fourier Transforms (FFTs) using a Hamming window with 50% overlap, giving the spectra 32 degrees of freedom. The horizontal spectra were used to calculate the sea surface elevation power spectral density using known depth and linear wave theory with the equation:

$$E(\sigma) = \frac{(S_{uu} + S_{vv})c^2}{g^2} \tag{2.3}$$

where $E(\sigma)$ is the sea surface elevation power spectral density, S_{uu} are S_{vv} are the horizontal velocity spectra, c is the wave celerity, and g is acceleration due to gravity. Because SWIFT measurements are Lagrangian, σ is the moving frame 'intrinsic' frequency, not to be confused with absolute frequency ω (Equation 1.7). Wave spectra are checked in bulk processing after daily deployments. Spectra giving a significant wave height of less than 0.25 m, are rejected due to noise concerns. Spectra with a peak frequency greater than 0.5 Hz are thrown out, because noisy low frequency components amplified by the conversion from orbitals to sea surface elevation (Equation 2.3) can inflate the estimate of H_s.

Peak wave direction, θ, is found using the a_2 and b_2 spectral coefficients, which are estimated from the equations: $a_2 = \frac{S_{uu}-S_{vv}}{S_{uu}+S_{vv}}$, and $b_2 = \frac{2C_{uv}}{S_{uu}+S_{vv}}$ where C_{uv} is the co-spectrum of the two horizontal velocity components. The direction is then found using the relation $\tan(2\theta) = \frac{b_2}{a_2}$, and therefore has 180 degree ambiguity because of the factor of 2 inside the tangent function. Wave directions are assumed to be propagating towards shore, but directions near grazing to shore can be difficult to analyze.

A comparison of SWIFT spectra with spectra from bottom mounted pressure sensors from a fixed array (data courtesy of Britt Raubenheimer and Steve Elgar) maintained for the duration of the New River Inlet experiment is shown in Figure 2.3. SWIFT spectra show good agreement with the fixed array sensors. The offshore measurements of the SWIFT and the array both agree with the Datawell Waverider located further offshore in 11m water depth. Comparisons are made in wavenumber space, as the fixed array instruments measure absolute frequency ω while the SWIFT measures intrinsic frequency σ. Although the comparison shows good agreement in heights and peak wavenumbers, small differences are expected, as the times and locations between the moving SWIFT and stationary instruments are not exactly matched. In addition, the SWIFT spectra made from 5 minute bursts may measure real differences when compared to the 1 hour bursts used in the fixed array spectra, as wave conditions may change over the course of an hour.

Currents are measured from the onboard GPS data, and averaged over the same 5 minute

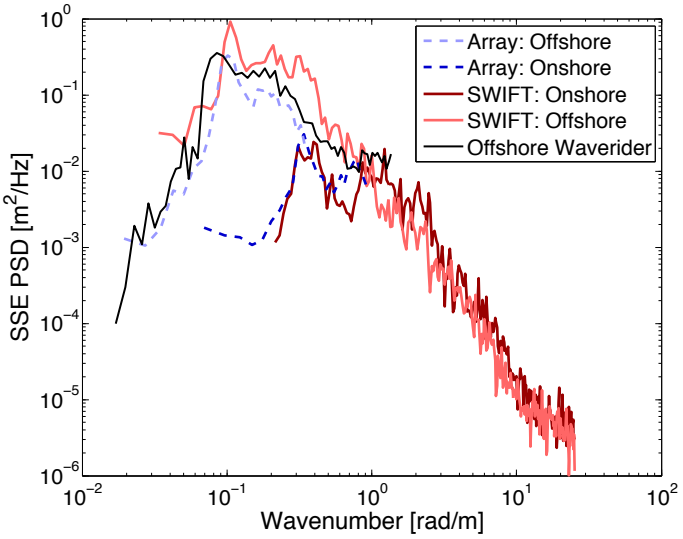

Figure 2.3: Comparison of SWIFT 5 minute spectra with 1 hour spectra from pressure data of the collocated array on May 2nd. The comparison is made in wavenumber space to avoid confusion between the absolute frequency ω, and intrinsic frequency σ

intervals as the wave spectra. The SWIFT drift speeds are slightly affected by wind drag, approximately 5% of the wind speed (Thomson, 2012). Reported currents are compensated for this 5% wind slip using data from the onboard anemometer.

2.2.2 Turbulent dissipation rates

Dissipation rates are calculated using a one sided, top down, second order structure function method: a direct eddy scale approach described in Wiles et al. (2006); Gemmrich (2010); Thomson (2012). The method follows the theory proposed by Kolmogorov (1941) and is based on the assumption that the second order structure function, $D(z,r)$, defined as:

$$D(z,r) =< \left(u'(z) - u'(z+r)\right)^2 > \tag{2.4}$$

scales with the squared velocity scale of turbulent eddies, s'^2, at a distance r. In the above equation $u'(z)$ is the turbulent velocity measured by the Aquadopp HR at a depth from the surface z, and r is the distance between the measurements, assumed to be the

eddy scale.

Kolmogorov hypothesized that the energy dissipation due to turbulence occurs at the smallest scales of turbulent motion. However, because energy in a turbulent flow field transfers from large scales to smaller scales, and energy enters a turbulent flow field at large scales, Kolmogorov hypothesized that the rate of turbulent energy dissipation can be related to the rate of energy exchange at larger scales (more specifically the inertial subrange). Using scaling analysis, Kolmogorov determined the second order structure function $D(z,r)$ is related to dissipation rate ϵ with:

$$D(z,r) = C_n^2 \epsilon^{\frac{2}{3}} r^{\frac{2}{3}} \tag{2.5}$$

where $C_n^2 = 2.1$ is a constant (Rusello and Cowen, 2011). Structure function values calculated from SWIFT velocity data are fit to $r^{\frac{2}{3}}$ using MATLAB's robust fit algorithm Holland and Welsch (1977) giving a slope A and an intercept N:

$$D(z,r) = A(z) r^{\frac{2}{3}} + N \tag{2.6}$$

Intercept values N are expected to follow a Gaussian distribution related to the noise in the velocity measurement. See Appendix A for a discussion on the errors associated with the second order structure function method. Dissipation rates ϵ can be estimated from the slope coefficients A at every depth z using:

$$\epsilon_{TKE}(z) = C_n^{-3} A(z)^{\frac{3}{2}} \tag{2.7}$$

Figure 2.4 shows an example of structure function fits to $r^{\frac{2}{3}}$ and the resulting dissipation rate profiles, taken from the SWIFT methods paper (Thomson et al., 2012). Figure 2.4 **a** and **b** show linear fits between $D(z,r)$ and $r^{\frac{2}{3}}$ as described in Equation 2.6. The structure function is well correlated with $r^{\frac{2}{3}}$ in both cases. Intercepts fall within the expected range for doppler noise, designated by the black triangle. Figure 2.4 **c** and **d** show the resulting dissipation rate profiles found using Equation 2.7. Dissipation rate profiles are largest near the surface and decay rapidly with depth, consistent with theory and previous studies (Craig and Banner, 1994; Terray et al., 1996; Gemmrich and Farmer, 2004).

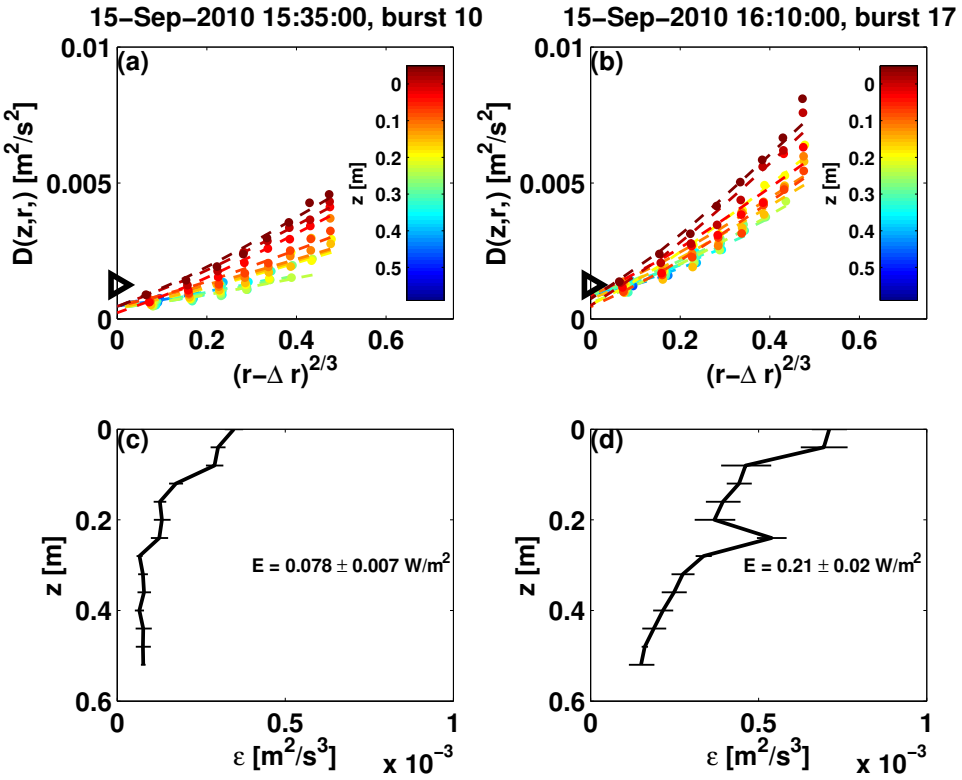

Figure 2.4: Two examples of structure function fits to $r^{\frac{2}{3}}$ with the resulting dissipation rate profiles are shown above. **(a)** and **(b)** show linear fits between the structure function and $r^{\frac{2}{3}}$. Separation distances $(r - \Delta r)$ are used to correct for platform motion. The slope of the best fit line, $A(z)$ is used to estimate dissipation rates $\epsilon(z)$ in **(c)** and **(d)**. Examples taken from the SWIFT methods paper (Thomson et al., 2012).

Another method commonly used to estimate dissipation is founded on the same arguments relating the rate of energy transfer in the inertial subrange to the dissipation rate. Using scaling analysis, the turbulent kinetic energy $E_{turb} = \frac{1}{2}u'^2$ is related to the dissipation in a wavenumber spectrum by $E_{turb}(k) = C_1\epsilon^{\frac{2}{3}}k^{\frac{-5}{3}}$. This method is often called the five thirds method due to the exponent of the wavenumber, k. The $k^{\frac{-5}{3}}$ dependence is expected only for the inertial subrange, and part of the challenge of this method is identifying the inertial subrange in the wavenumber spectrum. Making wavenumber spectra of turbulence is difficult because it requires accurate, coherent velocity measurements at multiple spatial locations. Therefore, it is common to take point measurements of velocity collected at a high frequency, and transpose it to a wavenumber. This is accomplished by assuming an advective velocity, U, for the turbulence, and relating frequent to wavenumber by $\frac{f}{U} = k$. All three methods of estimating dissipation rates are commonly used **?**. The advantage of the structure function method is that it allows for estimates of dissipation rate as a function of depth. SWIFT Dissipation rates estimated from the structure function method were found to agree to dissipation rates estimated using the Taylor's frozen turbulence method in an earlier study Thomson et al. (2012).

2.2.3 Breaking Rates

Breaking waves were counted by manual review of GoPro 1Hz images to calculate a breaking rate for each 5 minute burst. Only waves breaking over, or extremely close to (approximately less than 2m), the SWIFT hull were counted. Because the manual review of breaking rates is time consuming and automated methods are still under development, a select few tracks were counted (8 tracks total). GoPro clocks were synced before each deployment with visual images of wristwatches. These were confirmed with written records of SWIFT deployment times in order to sync GoPro timestamps with the GPS time recorded onboard. An example of a breaking wave image captured by the GoPro is shown in Figure 2.5. Images were not rectified, and no reference size was available in GoPro images and therefore no objective information about the size of breaking waves counted by the GoPro was drawn from the images. Therefore, while breaking rates are expected to correspond with increased

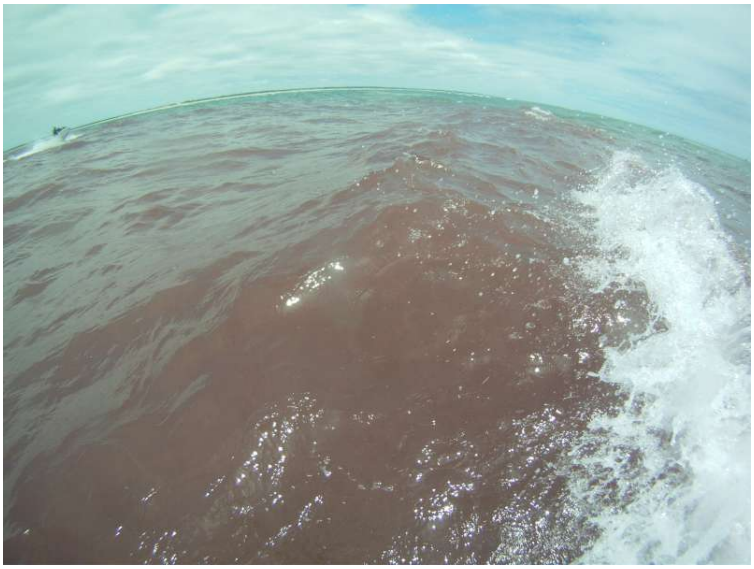

Figure 2.5: An example GoPro image with a breaking wave. The discoloration of the water surface was due to a rhodamine dye release earlier that day.

dissipation rates and changes in wave energy flux, the magnitude of these breaking proxies with respect to breaking rates varied, as small breaking waves and large breaking waves were counted alike.

Unlike surf zones at beaches with straight coastlines with shallow bottom slopes where bores are often well formed from the break point until the shore, the breaking regions at New River Inlet were often narrowly confined and would shift as modulated by the tides. Although increases in measured dissipation rate and a sharp decrease in wave energy flux are indications of wave breaking, visual confirmation of breaking points by images is useful to remove ambiguity. SWIFTs passing through a breaking region often counted fewer breaking crests than expected for the breaking region. As a result, the change in wave energy flux could indicate wave breaking while measured turbulent dissipation rates remained low. Images reviewed for the subset of tracks are therefore used as as confirmation for wave breaking predictors that are later applied to the larger data set.

Chapter 3

RESULTS

3.1 Selected Tracks (8 tracks)

SWIFT drift tracks which have processed video data are shown in Figure 2.1b. SWIFTs deployed on ebb tides from inside the inlet (green tracks in Figure 2.1b) preferentially followed the channels out the inlet and once offshore they followed the wind and wave directions. Breaking on ebb tides was observed at the ends of channels where currents were large (Figure 2.1a). Breaking on ebb tides also occurred over the shallow shoals near North Topsail Island and Onslo Beach.

Flood deployments (magenta tracks in Figure 2.1b) resulted in a more diffuse pattern, in which SWIFTs would rarely drift into the inlet when dropped more than approximately 700m from the river mouth. Breaking on flood tides occurred primarily on the shoals near North Topsail Island and Onslo Beach, and the shallow bar in between the two dredged channels.

3.1.1 Ebb example

Figure 3.1 shows an example ebb drift track from May 20th, 2012. Three independent wave breaking metrics, wave energy flux gradient, dissipation rates, and breaking counts, all indicate breaking at approximately 1000m along track (panels a,b,c). Panel (a) shows wave energy flux is constant offshore, increasing against the ebb current at the channel mouth, then declining to near zero from breaking. Wave focusing due to currents, the process attributed to increasing energy flux before the break point, is discussed in Appendix B. Panel (b) confirms visual identification of breaking waves using the onboard camera. Panel (c) shows an increase in turbulent dissipation rates coincident with both observed breakers and a change in wave energy flux. Panel (d) of Figure 3.1 shows three non-dimensional parameters relevant to this process: γ, γ_u, and Fr. The breakpoint value of γ is low

($\gamma \approx 0.2$) compared to published values of γ, which are in the range 0.3 to 0.8 for most breakpoints. In contrast, the breakpoint value of the new parameter γ_u is higher ($\gamma_u \approx 0.3$) and within the range of nominal breakpoint values, because it accounts for the opposing currents.

The Froude number Fr, often used to prescribe wave blocking by currents, is shown to be ineffective at prescribing wave breaking in panel (d) of Figure 3.1. This is because Fr does not include any information about wave height (or steepness), and thus any wave in a strong current can have a high Fr. In this and other ebb examples Fr is maximum inside the inlet, decreases over the break point, and is near zero offshore. Therefore no critical value exists to diagnose a breakpoint, as Fr was often maximum in in the presence of very small waves.

3.1.2 Flood example

Figure 3.2 shows an example flood track for which the SWIFT was deployed offshore and drifted into the inlet. A breakpoint is identified between along track distances 500m and 1000m, using the decrease in wave energy flux in panel (a), the camera breaking counts in panel (b), and the elevated turbulent dissipation rates in panel (c). The value of the depth limited breaking parameter, γ, is larger than expected at the break point ($\gamma \approx 0.4$), especially when compared with the ebb example shown in Figure 3.1 (for which $\gamma \approx 0.2$ at breakpoint). The modulation of the critical value of γ by currents can be seen by contrasting these two examples. The inclusion of currents in the new parameter γ_u yields a more consistent critical break point value between the flood and ebb examples, both of which show breaking at $\gamma_u \approx 0.3$. In both examples, the $\cos\theta$ in Eq. 2.2 is taken to be $\mathrm{sgn}(\cos\theta)$ (i.e. ± 1), as the errors in measured wave directions are large. This simplifies the formulation to $\gamma_u = \frac{Hg}{(\sqrt{gd} \pm U)^2}$. This assumption is evaluated in the following section.

3.1.3 Evaluation of γ_u

In an idealized case, breaking parameters are binary; any subcritical value is non-breaking, any critical value is breaking, and super-critical values do not exist (since the act of break-

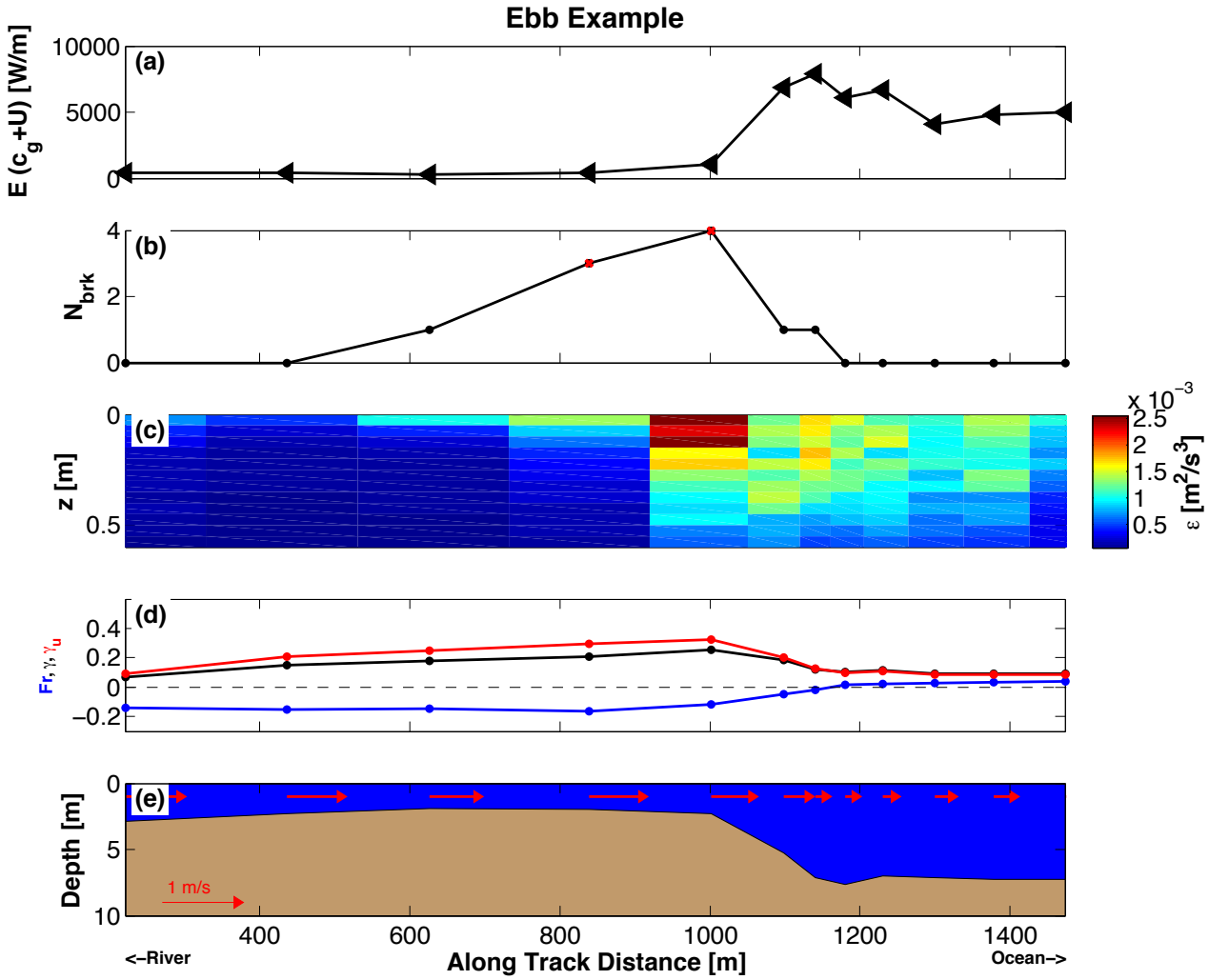

Figure 3.1: Example ebb SWIFT drift on May 20th, 2012. The SWIFT was deployed inside the inlet (left) and drifted offshore (right) as time progressed. Panel **(a)** shows wave energy flux. Panel **(b)** shows breaking count from onboard images. Panel **(c)** shows turbulent dissipation rate beneath the waves. Panel **(d)** shows three non-dimensional parameters. Panel **(e)** shows the bathymetry and the measurement tidal currents (scaled arrows).

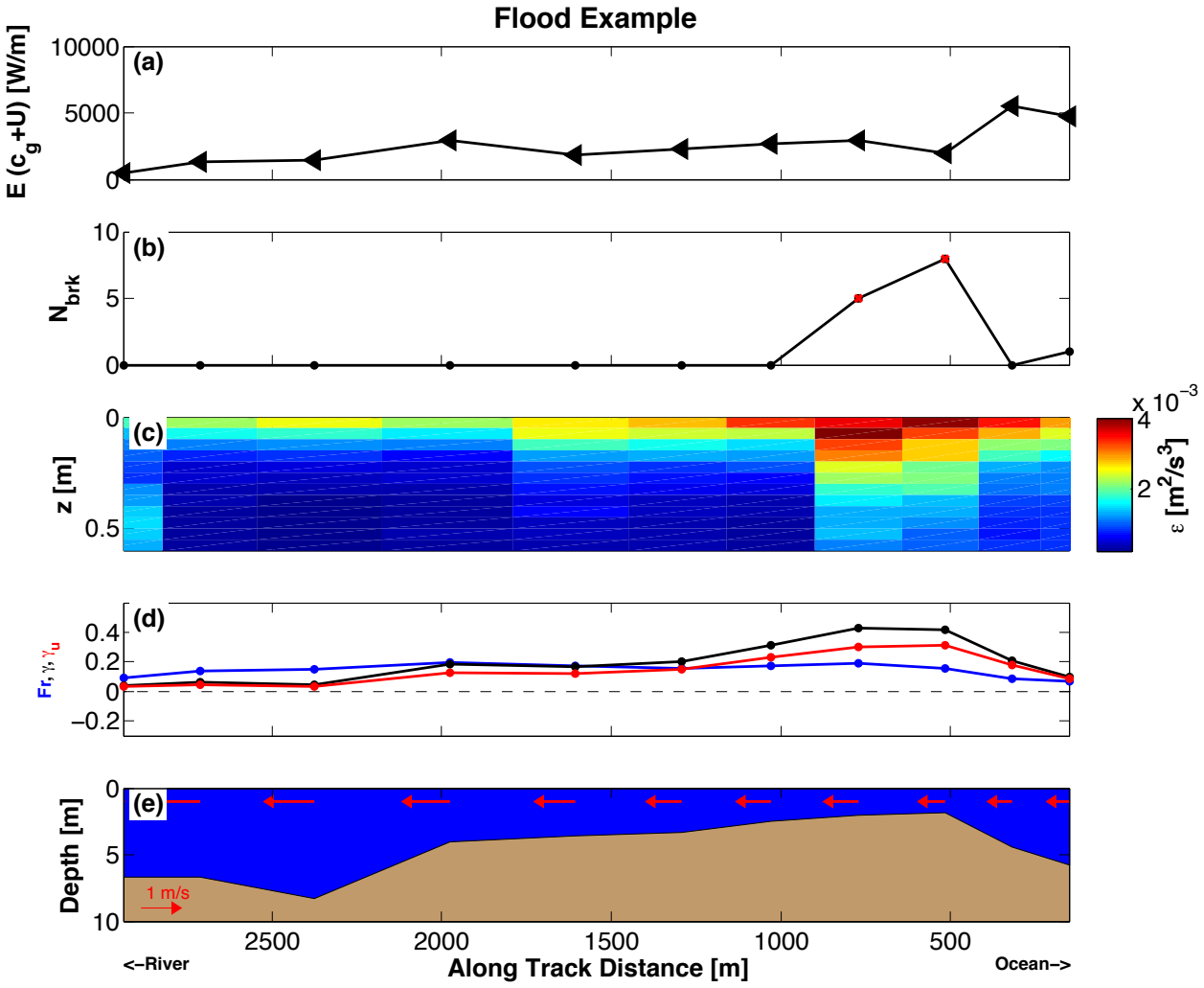

Figure 3.2: Example flood SWIFT drift on May 13th, 2012. The SWIFT was deployed offshore (right) and drifted into the river inlet (left). Panel **(a)** shows wave energy flux. Panel **(b)** shows breaking count from onboard images. Panel **(c)** shows turbulent dissipation rate beneath the waves. Panel **(d)** shows three non-dimensional parameters. Panel **(e)** shows the bathymetry and the measurement tidal currents (scaled arrows).

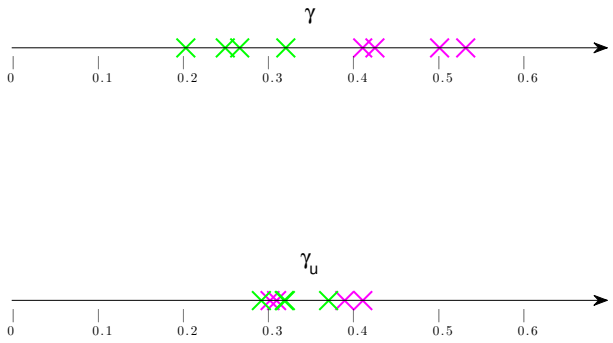

Figure 3.3: Values of γ and γ_u at the break point. Green x's represent data collected on ebb tides when waves oppose currents. Magenta x's represent data collected on flood tides when waves follow currents. The sign of $\cos\theta$ was used instead of the value when calculating γ_u (Equation 2.2) because wave directions were mostly collinear with the currents. The range of γ is larger than γ_u. (See Table 3.1 for actual values.)

ing is a limiting processes). Uncertainties in measurements and secondary processes add variability to breaking parameters such that idealized critical values for breakpoint identification are never absolute, but they can still be useful. Three factors can be considered in the utility of the determined critical value of a breaking parameter: 1) minimal false positives (i.e., non-breaking waves at the critical value), 2) maximum true positives (i.e., correct identification of breaking waves at the critical value), and 3) minimal super critical values. The parameters γ and γ_u are tested for these three criterion below, using the eight selected tracks shown in Figure 1b.

The ebb and flood example tracks of Figures 3.1 & 3.2 showed that γ_u can have a consistent breakpoint value in the presence of currents, while the conventional γ varies. Results from six other camera-identified breakpoints (totaling eight tracks and eight breakpoints shown in Figure 2.1) further show that γ_u has less variability at the break point than γ. The breakpoint values are shown in Figure 3.3 and Table 3.1. The mean breakpoint value of both parameters is similar (0.37 and 0.34), but the range of γ_u is much smaller than that of γ. Thus, applying a γ_u criterion is expected to improve breaking prescription, relative to a conventional γ criterion.

Critical values of γ are distinctly separated by tide stage such that any given ebb value is

Table 3.1: Values of γ and γ_u at break points.

γ	γ_u	Break point time
0.21	0.29	20-May-2012 12:37:07
0.25	0.32	20-May-2012 12:42:07
0.27	0.32	17-May-2012 11:17:07
0.32	0.37	17-May-2012 12:02:07
0.54	0.41	18-May-2012 07:52:07
0.51	0.39	13-May-2012 13:12:07
0.42	0.31	13-May-2012 13:02:07
0.43	0.30	13-May-2012 13:07:07
0.37 $\pm$ 0.33	0.34 $\pm$ 0.12	Mean $\pm$ Range

less than any given flood value. This is expected because opposing currents cause breaking to happen in deeper water and following currents cause breaking to happen in shallower water. The new parameter γ_u incorporates this current information and therefore has a critical value that is more consistent across all cases, unbiased by tide stage. On floods (magenta) the sign of U is positive such that larger U reduces the value of γ_u. On ebb tides (green), larger values of U increase the value of γ_u accounting for the increase in steepness due to opposing currents.

3.2 Full Data Set (500 tracks)

More data than the 8 sample tracks are needed to evaluate how the different breaking parameters perform on false positives (i.e. non-breaking waves at a measured critical value) and super critical values (there should be few or none), . Extending the comparison of γ versus γ_u to the entire data set requires the use of one of the other breaking measurements, as manual review of images along all 500 tracks is not feasible. Measured turbulent dissipation rates normalized by wave energy flux gradients were used to evaluate γ versus γ_u for the full data set (Figure 3.4). Physically, this normalized metric is the fraction of the wave energy

flux that is being dissipated by turbulence at a given location. This is both an indicator of breaking and a proxy for breaker strength. This metric is shown to have substantially separated average profiles between breaking and non-breaking cases in the 8 example tracks for which breaking is identified by video (Figure 3.4).

A critical value of 0.35 was used in Figure 3.4, determined from the mean value of γ and γ_u (Figure, 3.3, Table 3.1), and from Figure 3.5. For comparison, the critical value at a nearby site, Duck, NC, is $\gamma \approx 0.45$ (e.g. Sallenger Jr. and Holman (1985), $\gamma_{rms} = 0.32$,). Mean critical profiles of γ_u were not sensitive to small changes in the prescribed critical value as shown in Table 3.2. Mean critical profiles of γ showed more variation across a range of critical values, but in each case the normalized dissipation was lower than γ_u.

A successful breaking parameter should have a notable difference of normalized dissipation rates when separated between sub-critical and critical cases. Figure 3.4 shows increased separation of turbulent dissipation rate profiles when all 500 tracks are grouped and averaged as sub-critical and critical, for both γ and γ_u. The γ_u separation is greater, however, than the γ separation, and this suggests that there are fewer false-positives in the γ_u categorized results. That γ and γ_u categorized profiles are similar is expected, given that most of the breaking is still largely controlled by depth shoaling.

The total turbulent dissipation (as opposed to the depth profiles used in Figure 3.4) is similarly normalized by wave energy flux gradients and used to evaluate the underlying assumption of criticality in the γ and γ_u parameters. Figure 3.5 shows the normalized total dissipation rates increase with γ_u until the previously determined critical value of 0.35, above which there are very few measurements (i.e., very few observations of super-critical γ_u, most of which are likely attributed to measurement error). In contrast, the normalized total dissipation rates do not follow a simple pattern as a function of γ. Rather, there is a spike in dissipation at $\gamma \approx 0.22$, then a local minima, followed by another spike at $\gamma \approx 0.44$. This indicates breaking occurring for an inconsistent set of γ values.

The slightly increased normalized dissipation rates occurring at the lowest two bins of both γ, and γ_u in Figure 3.5 is attributed to problems in the normalization scheme for small values (i.e., where low values of available wave energy flux combine with dissipation rates related to non-breaking mechanisms). This signal-to-noise issue occurs inside the inlet where

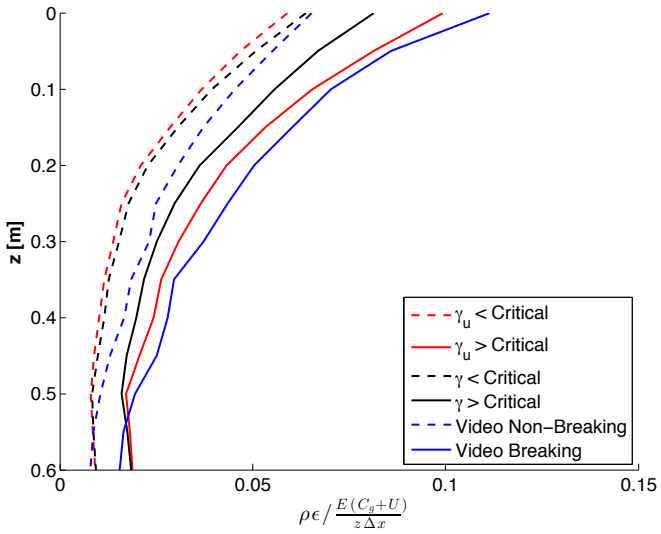

Figure 3.4: Turbulent dissipation rate profiles averaged together in two categories, above critical and below critical values , each for γ (black) and γ_u (red). A critical value of 0.35 was used, although results shown in Table 3.2 show low sensitivity to variations of the critical value. Profiles are conditioned for $|U| > 0.5$ m/s because for low currents $\gamma \approx \gamma_u$. Profiles with wind speeds greater than 5 m/s are also excluded to reduce whitecap effects. Turbulent dissipation rate profiles were normalized by available wave energy flux because the range of offshore waves conditions varied during the experiment, and larger waves sampled on flood would otherwise bias flood dissipation rates high. 330 profiles were averaged together for the mean subcritical profile, and 100 for the mean supercritical profile. Standard errors for the profiles ranged between 15% and 20%.

Table 3.2: Average critical dissipation values, depth integrated and normalized ($\epsilon* = \rho \int \epsilon dz / \frac{E(C_g+U)}{\Delta x}$) for critical values of γ and γ_u.

Critical Value	ϵ^* for $\gamma >$ Critical Value	ϵ^* for $\gamma_u >$ Critical Value
0.33	0.033	0.040
0.34	0.032	0.040
0.35	0.033	0.040
0.36	0.035	0.040
0.37	0.037	0.040
0.45 (Liturature: Duck NC)	0.037	[-]

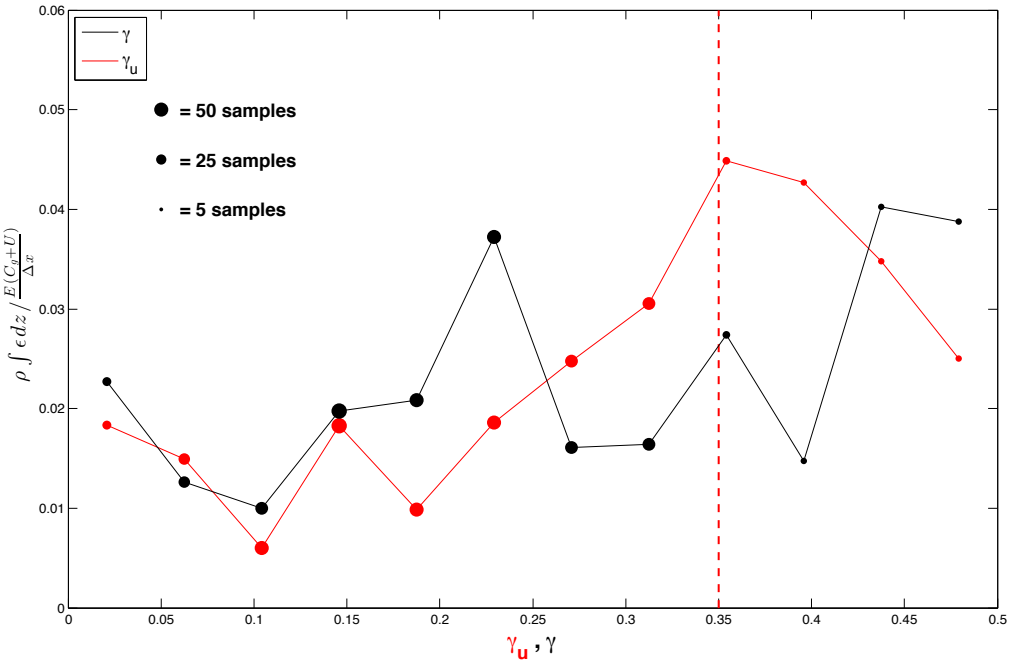

Figure 3.5: Depth averaged dissipation rates normalized by available wave energy flux versus the breaking parameters γ (black) and γ_u (red). The area of the circle represents the number of samples included in the bin average, from a total of 330 samples. The dashed red line represents the critical value of γ_u.

turbulence from channel features and low wave energy flux are expected. This is therefore an artifact of the breaking proxy and not indicative of breaking parameter performance.

3.3 Fixed Array

Fixed array data was provided by Britt Raubenheimer and Steve Elgar in order to compare SWIFT measurements. A SWIFT typically passes across the surf zone during a deployment, and thus sees the initial break point. Initiation of breaking would rarely occur directly over the array's instruments, despite their number. Histograms of the two breaking parameters γ and γ_u made from fixed array data is shown in Figure 3.6. Only data from instruments close in space and time to the SWIFT tracks shown in Figures 3.1 and 3.2 are used to make the histograms. The SWIFT drifters observed breaking during the example drifts as confirmed by three independent breaking metrics. Therefore, it is expected that the fixed instruments near the breaking locations observed in the SWIFT tracks should have similar near critical breaking parameters. The histograms in Figure 3.6 show subcritical values ($\gamma.\gamma_u < 0.35$) of both breaking parameters, indicating that no breaking is observed by the fixed array. This is not inconsistent with the collocated SWIFT results, but it implies breaking occurring in between fixed array sensors. This indicates that a full evaluation of γ and γ_u using the fixed array would require external confirmation of co-located wave breaking (such as by the ARGUS or infrared cameras also deployed during the NRI experiment).

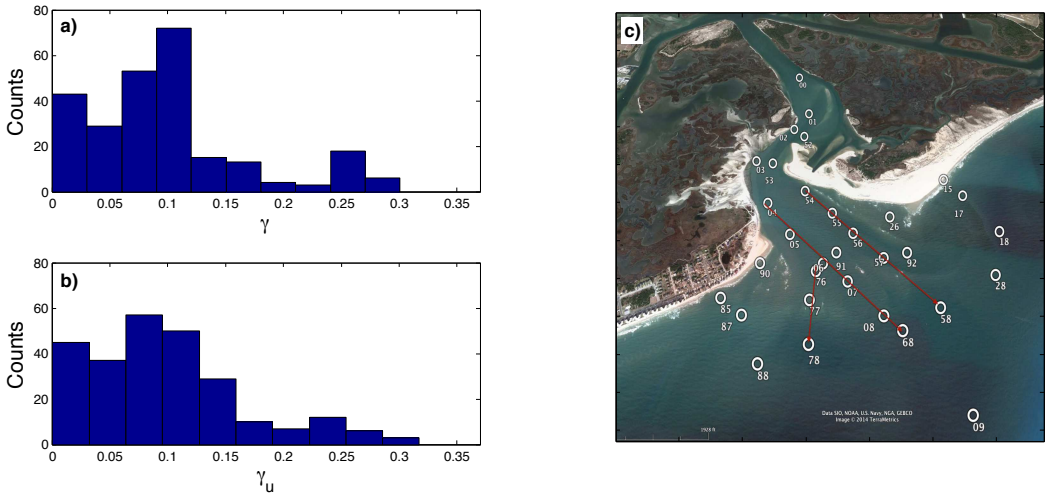

Figure 3.6: Histograms of γ **(a)** and γ_u **(b)** from fixed array pressure sensors and ADVs **(c)** located near the example SWIFT flood and ebb tracks in space and time. The data from the fixed sensors were averaged over 512s intervals. The full array of sensors is shown, but only data from instruments close to the SWIFT tracks shown in Figures 3.1 and 3.2 is used to make the histograms.

Chapter 4

DISCUSSION AND INTERPRETATION

4.1 Breaking Parameters

The new parameter γ_u is shown to be effective in shallow water, where it successfully captures the modulation of depth-limited breaking by currents. However, γ_u has not been tested for intermediate and deep water cases. Indeed, while γ retains the relation to Miche's steepness criterion in deep water, γ_u does not have a similar deep water form. Still, the new parameter may prove useful for predicting intermediate and deep water wave-current breaking. To illustrate this point, consider the wave blocking case $\frac{U}{C_p} = -\frac{1}{2}$ limit from Mei (1989). For deep water, $C_p = 2C_g$, therefore γ_u is asymptotic on an opposing current when $U = -C_g$. For shorter waves (T$< 1s$), this limit can still be reached and critical values of γ_u might be seen in deep water.

A current oblique to the incoming waves will not significantly increase γ_u, as the $\cos\theta$ selects only the proportion of the current in the direction of the wave, consistent with the vector wave action balance and with the vector adjustment of intrinsic and absolute frequencies via $\vec{u} \cdot \vec{k}$ (Equation 1.7). However, gradients in the currents (which are common at inlet mouths) will refract waves to face the currents, such that γ_u will increase. A continued discussion of refraction can be found in Appendix B.

Both γ_u and γ are sensitive to errors in depth, but γ_u is also sensitive to the angle between the currents and the waves, as the cosine function is sensitive to errors in θ. In cases where the angle is not well determined, using a reduced form without the cosine term is recommended. In shallow water, this is simply $\gamma_u = \frac{Hg}{(\sqrt{gd} \pm U)^2}$.

Raubenheimer et al. (1996) showed that the critical value of γ was a function of beach slope β such that $\gamma_{brk} = C_0 + C_1 \frac{\beta}{kd}$. While this form was not tested in the current study, the critical value of γ_u could also be adjusted for beach slope. For large kd (deep water), this slope would be negligible.

The new parameter γ_u can be rearranged in form to resemble the γ formulation in Raubenheimer et al. (1996). Taking the defined,$\gamma_u = \frac{H_s g}{(C_g + U\cos\theta)^2}$ and expressing the right hand side as $\frac{H_s}{d}$ yields:

$$\gamma = \gamma_u(\frac{C_g}{\sqrt{gd}} + \frac{U\cos\theta}{\sqrt{gd}})^2$$

. In shallow water this reduces to:

$$\gamma = \gamma_u(1 + Fr)^2 \tag{4.1}$$

where Fr is the signed Froude number. This shows that γ is a quadratic function of the Froude Number, related by the constant γ_u. This form can be more easily integrated into existing models that use γ as an input (e.g. the Miche (1954) steepness model, the Thornton and Guza (1983) dissipation model, and others).

4.2 Turbulence and Breaking

The wave energy lost during breaking is often assumed to be dissipated in a turbulent cascade. The results of Figure 3.5, however, show that SWIFT measurements of turbulent dissipation rates, when depth-integrated, are only a small fraction (1-10%) of the change in wave energy flux. This small fraction is qualitatively consistent with Feddersen (2012) and with Thomson (2012) who found depth-integrated dissipation rates to be ∼1% of the change in wave energy flux. This result is further investigated by evaluating some of the terms in a budget for turbulent kinetic energy TKE, which is can be posed as

$$\frac{D}{Dt}\left(\int TKE dz\right) = P_{TKE} - \epsilon_{TKE} - T, \tag{4.2}$$

where $\frac{D}{Dt}$ is the material derivative (which includes transport by the mean flow), P_{TKE} is production of TKE, ϵ_{TKE} is the dissipation of TKE, and T is the transport of TKE by the turbulence itself. Because the SWIFT moves with mean currents, the material derivative on the left hand side of Equation 4.2 is taken to be the measured change in TKE over time from the SWIFT reference frame. The SWIFT is constrained to the surface, so TKE can still advect downwards out of the control volume. This downward advection of TKE is not

measured. In addition, the self-transport of turbulence out of the control volume, T, is not measured.

TKE production P_{TKE} can be prescribed as the wave energy loss as measured by the GPS-based wave measurements onboard the SWIFT. Of course, not all wave energy becomes TKE, and a full account on the energy must also include the MKE (mean kinetic energy) of currents and the work done on bubbles (i.e., buoyancy B). Thus,

$$P_{TKE} = \frac{\partial}{\partial x} E(C_g + U) \left(\frac{N_{break}}{\sigma_{peak} \delta t} \right) - \frac{\partial MKE}{\partial t} - B, \tag{4.3}$$

where N_{break} is the number of observed breaking waves, σ_{peak} is the intrinsic peak wave frequency, and $\delta t = 300s$ is the five minute burst interval. We assume shallow water $C_g = \sqrt{gd}$ and note the lack of estimates for MKE and B from our measurements. The spacial gradient $\frac{\partial}{\partial x}$ is estimated using a centered difference between the previous and subsequent burst averages. The term $\frac{N_{break}}{\sigma_{peak} \delta t}$ is a correction factor needed to compare the statistical average of change in energy flux to the production seen in the SWIFT's control volume. Assuming a monochromatic wave at a peak frequency ω_{peak}, and loss of wave energy flux (i.e. production) is evenly distributed among each breaking crest, then the TKE production measured by the SWIFT is expected match only the energy flux lost from crests that break over, or very near the SWIFT. In other words, the correction term $\frac{N_{break}}{\sigma_{peak} \delta t}$ is the fraction of change in energy flux per wave crest, multiplied by the number of breaking crests seen by the SWIFT (i.e. the fraction of wave energy dissipation expected to be observed by the SWIFT). The intrinsic measured peak frequency σ_{peak} is used in the correction term rather than the absolute peak frequency ω_{peak} so that $\sigma_{peak} \delta t$ approximates the total number of wave crests seen by the SWIFT in the $\delta t = 300$s burst average.

Figure 4.1 shows an along track balance of $\frac{D}{Dt} \left(\int TKE dz \right)$ with $P - \epsilon_{TKE}$ for the example ebb SWIFT track shown in Figure 3.1. The correlation between the two curves is approximately 0.7, with the change in TKE approximately much smaller (about $\frac{1}{50}$) than the size of the $P - \epsilon_{TKE}$ term. The elevated dissipation of TKE for hundreds of meters past the break point suggests that advection of TKE may be a leading order term in the TKE budget. If strong TKE dissipation continues to occur long after the TKE has moved away

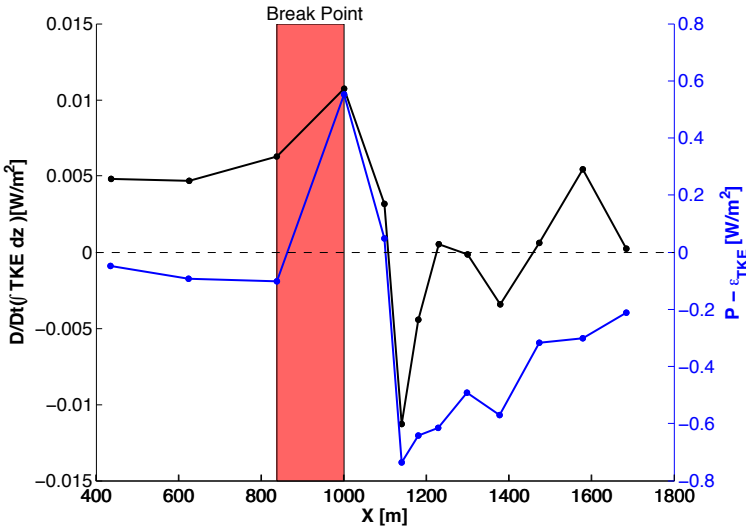

Figure 4.1: Select terms from the TKE budget for the example ebb SWIFT track shown in Figure 3.1. Spacing of points along the x-axis is not uniform, as the drift speed changed over the deployment. The transparent red box indicates the breakpoint.

from the breakpoint, then much of the "missing" dissipation in Feddersen (2012) or Thomson (2012) might be a local imbalance of production and dissipation. It should be noted that the local imbalance between production and dissipation is not accounted for by local change in TKE. At the break point, generation of bubbles, sound, and MKE are expected to account for the extra production, but offshore the imbalance between dissipation of TKE and change in TKE is unexpected.

Along track integrated $P-\epsilon_{TKE}$ is $-260\frac{W}{m}$, which accounts for approximately all but 4% of the $5000\frac{W}{m}$ offshore wave energy flux. The negative sign of the result implies the SWIFT measured more dissipation of TKE than production. This "missing" production is likely due to errors in the production correction term. The assumptions of a monochromatic wave does not account for processes such as wave groups, which spread energy unevenly across wave crests during the SWIFT's 5 minute averaging period. The term is also sensitive to the choice of peak frequency σ_{peak}, which was not always well defined from the SWIFT's 5 minute spectra. In addition, error analysis on the turbulence measurements (discussed in

detail in Appendix A) suggest doppler noise may bias dissipation rate estimates high.

Figure 4.1 is shown as an example, but not all tracks showed such a correlation. There was often too much noise in the wave energy flux for a clean gradient. Turbulence input from non-breaking sources also adds noise in this formulation of the TKE budget. In spite of this, the example is useful to show the importance of breakpoint location and advective processes in nearshore TKE dynamics. Advection is important both because of strong currents, and because the dissipation of turbulence (i.e., the theoretical cascade) requires time and space. Thus it is not surprising that a local balance of turbulence production and turbulence dissipation has yet to be observed in shallow wave breaking conditions.

4.3 Wind Effects

In contrast to the shallow-water results, the offshore data suggest that turbulent dissipation achieves a local balance with production of turbulence, for which whitecaps forced by surface winds are the dominant mechanism. Figure 4.2 shows an example drift track offshore of the inlet where the TKE dissipation rate is balanced by wind input as described in Equation 1.8. Dissipation rates were larger than the wind input, consistent with advection of turbulence on ebb tides offshore of the inlet. There were no long deployments in deep water on flood tides, since SWIFTs that did not enter the inlet were recovered and reset.

The dependence of dissipation rate on wind input is not limited to one example. Figure 4.3 shows turbulent dissipation rate profiles bin averaged by wind speed for low values of γ used to identify offshore locations. The turbulent dissipation rate sorting with increased wind speed is consistent with results found in Thomson et al. (2013). The profile shape shows the most dramatic increase in dissipation very near the surface, within the top 30cm of the water column.

Although the wind effects can be seen most clearly using the data from offshore, where wind stress and whitecaps are the dominant mechanisms, wind is a likely source of scatter amongst the shallow-water results. This is a tertiary effect to the modulation of breaking by currents discussed earlier. Thus, we find that wave breaking and turbulence at a tidal inlet is controlled by depth, currents, and wind – in that order.

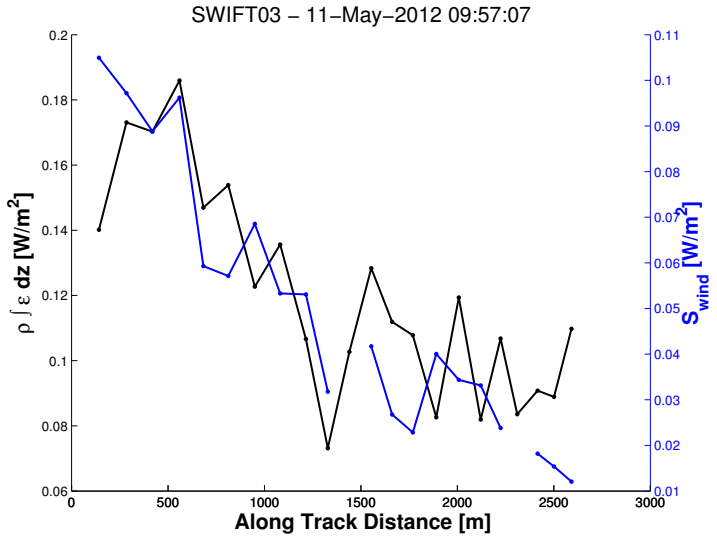

Figure 4.2: Depth averaged dissipation rates (black line) and wind energy input (blue line) versus along track distance. These values are offshore, in deep water ($\gamma < 0.1$) where a SWIFT was left to drift with the wind and waves. S_{wind} is calculated as formulated in Equation 1.8, using a phase speed estimated as the weighted average speed of wave period greater than 6 seconds.

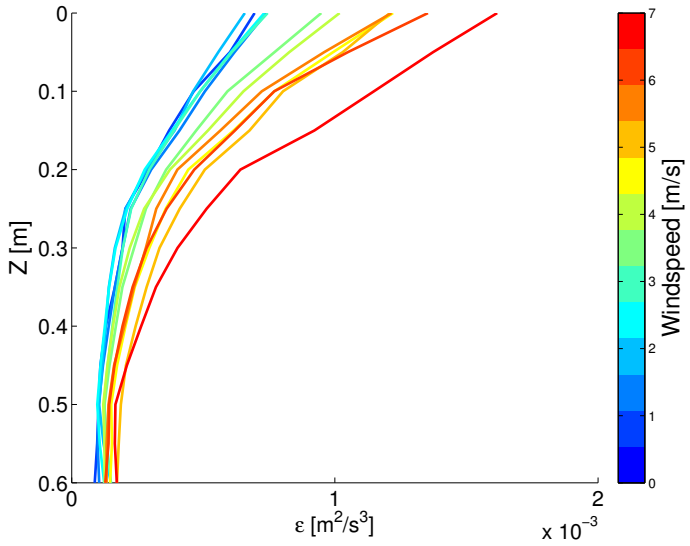

Figure 4.3: Turbulent dissipation rate profiles as a function of depth bin averaged by wind speed. Profiles are thresholded for depth and current limited wave breaking by using low values of γ. Dissipation rates increase with increased wind, with the most dramatic increases in the top 30cm os the water column.

Chapter 5

CONCLUSION

Wave breaking is examined at an inlet with strong tidal currents and waves incident from the open ocean. Drifter data shows visual identification of breaking corresponds with decreases in wave energy flux, increased turbulent dissipation rates, and is coincident with depth and current shoaling. The critical value of a conventional depth-limited breaking parameter γ varies with currents and does not accurately predict wave breaking. The critical value of new breaking parameter γ_u, based on adjustment of the wave propagation speed in the presence of currents, is a more consistent indictor of wave breaking. The critical value of γ_u also improves separation of the measured near surface turbulent dissipation rates associated with breaking (a proxy for breaking strength). An energy budget is evaluated where production is assigned from change in wave energy flux. Change of TKE following the mean current is shown to correlate well with production minus dissipation ($r^2 \approx 0.7$), but differ by over an order of magnitude. Elevated dissipation rates persisting beyond the break point are consistent with advection of turbulence by mean currents and may be important in a nearshore momentum balance. Dissipation rates are shown to increase with windspeed, consistent with increased white capping as see in previous studies.

Future work will examine wave breaking and turbulence at intermediate depths with vertically sheared currents using data collected at the Columbia River Mouth. Breaking at the Columbia River Mouth was observed in intermediate depths ($\frac{1}{20} < \frac{d}{L} < \frac{1}{2}$), with currents as strong as 3 ms^{-1}. The effects of currents on waves are therefore expected to be more important than bathymetry when compared to the New River Inlet, where bathymetry is still of primary importance. The new breaking parameter, γ_u, will be tested at the new site. In addition, the measurements will help study the effect of sheared currents on waves, which has been discussed analytically (e.g. Kirby and Chen (1989)), but for which limited in situ measurements exist.

BIBLIOGRAPHY

Battjes, J. A. and J. P. F. M. Janssen (1978). Energy loss and set-up due to breaking of random waves. *Proc. INt. Conf. Coastal Eng. 16th*, H569 – H587.

Bowen, A. J., D. L. Inman, and V. P. Simmons (1968). Wave 'set-down' and set-up. *Journal of Geophysical Research 73*(8), 2569–2577.

Chawla, A. and J. T. Kirby (2002). Monochromatic and random wave breaking at blocking points. *Journal of Geophysical Research 107*(C7).

Clark, D. B., L. Lenain, F. Feddersen, E. Boss, and R. Guza (2014). Aerial imaging of flourescent dye in the nearshore. *J. Atmos. Oceanic Tech.*.

Craig, P. D. and M. L. Banner (1994). Modeling wave-enhanced turbulence in the ocean surface layer. *J. Phys. Oceanogr. 24*, 2546–2559.

Demirbilek, Z. and C. L. Vincent (2008). Chapter ii: Water wave mechanics. *Coastal Engineering Manual*.

Elgar, S., T. H. C. Herbers, V. Chandran, and R. T. Guza (1995, March). Higher-order spectral analysis of nonlinear ocean surface gravity waves. *Journal of Geophysical Research 100*(C3), 4977–4983.

Feddersen, F. (2012, March). Observations of the surf-zone turbulent dissipation rate. *Journal of Physical Oceanography 42*, 386–399.

Freilich, M. H., R. T. Guza, and S. L. Elgar (1990). Observations of nonlinear effects in directional spectra of shoaling gravity waves. *Journal of Geophysical Research 95*(C6), 9645–9656.

Gallagher, E. L., S. Elgar, and R. T. Guza (1998). Observations of sand bar evolution on a natural beach. *Journal of Geophysical Research 103*(C2), 3203–3215.

Gemmrich, J. (2010, March). Strong turbulence in the wave crest region. *Journal of Physical Oceanography 40*, 583–595.

Gemmrich, J., T. Mudge, and V. Polonichko (1994). On the energy input from wind to surface waves. *J. Phys. Oceanogr. 24*, 2413–2417.

Gemmrich, J. R. and D. Farmer (2004). Near-surface turbulence in the presence of breaking waves. *J. Phys. Ocean. 34*, 1067–1086.

Gerkema, T., L. R. M. Maas, and H. van Haren (2012). A note on the role of mean flows in doppler-shifted frequencies. *Journal of Physical Oceanography 43*, 432–441.

Hayes, M. O. (1980). General morphology and sediment patterns in tidal inlets. *Sedimentary Geology 26*, 139–140.

Herbers, T. H. C., P. F. Jessen, T. T. Janssen, D. B. Colbert, and J. H. MacMahan (2012, July). Observing ocean surface waves with gps-tracked buoys. *Journal of Atmospheric and Oceanic Technology 29*, 944–959.

Herbers, T. H. C., N. R. Russnogle, and S. Elgar (2000). Spectral energy balance of breaking waves within the surf zone. *J. Phys. Oceanogr. 30*, 2723–2737.

Hoefl, F. and S. Elgar (2003, Mar.). Wave-induced sediment transport and sandbar migration. *Science 299*(5614), 1885–1887.

Holland, P. W. and R. Welsch (1977). Robust regression using iteratively reweighted least-squares. *Communications in Statistics: Theory and Methods A6*, 813–827.

Iverson, H. W. (1952). *Laboratory study of breakers, Gravity Waves.* Circ. 52, U.S. Bur. of Stand., Washington, D.C.

Kirby, J. T. (1984). A note on linear surface wave-current interation over slowly varying topography. *Journal of Geophysical Research.*

Kirby, J. T. and T. Chen (1989). Surface waves on vertically sheared flows: Aproximate dispersion relations. *Journal of Geophysical Research 94*(C1), 1013–1027.

Kolmogorov, A. N. (1941). Dissipation of energy in the locally isotropic turbulence. *Dokl. Akad. Nauk SSR 30*, 301–305.

Lamarre, E. and W. K. Melville (1991). Air entrainment and dissipaiton in breaking waves. *Letters to Nature 351*, 469–472.

Lippmann, T. C. and R. A. Holman (1990, July). The spatial and temporal variability of sand bar morphology. *Journal of Geophysical Research 95*(C7), 11575–11590.

Longuet-Higgins, M. S. (1970, November). Longshore currents generated by obliquely incident sea waves, 1. *Journal of Geophysical Research 75*(33), 6778–6789.

Méhauté, B. L., D. Divoky, and A. Lin (1968). Shallow water waves: A comparison of theories and experiments. *11th International Conference on Coastal Engineering, Am. Soc. of Civ. Eng., London*.

Mei, C. (1989). *The Applied Dynamics of Ocean Surface Waves*. Teaneck, NJ: World Scientific.

Melville, W. K. (1996). The role of surface-wave breaking in air-sea interaction. *Annu. Rev. Fluid Mech. 28*, 279–321.

Miche, R. (1954). Mouvements ondulatoires des mers en profondeur constante ou decroissante. *Univ. Calif. Berkeley Wave Re. Lab. Ser. 3*(363).

Munk, W. (1944). Proposed uniform procedure for observing waves and interpreting instrument records: Scripps institution of oceanography. *Wave Report No. 26*.

Nichols-Pagel, G., D. B. Percival, P. Reinhall, and J. Riley (2008). Should structure functions be used to estimate power laws in turbulence? *Physica D: Nonlinear Phenomena 237*(5), 665–77.

Phillips, O. M. (1985). Spectral and statistical properties of the equilibrium range in wind-generated gravity waves. *J. Fluid Mech. 156*, 495–531.

Raubenheimer, B., R. T. Guza, and S. Elgar (1996). Wave transformation across the inner surf zone. *Journal of Geophysical Research 101*(C10), 25589–25597.

Rusello, P. J. and E. Cowen (2011). Turbulent dissipation estimates from pulse coherent doppler instruments. In *Current, Waves and Turbulence Measurements (CWTM)*.

Sallenger Jr., A. H. and R. A. Holman (1985). Wave energy saturation on a natural beach of variable slope. *Journal of Geophysical Research 90*(C6), 11939–11944.

Terray, E., M. Donelan, Y. Agrawal, W. Drennan, K. Kahma, A. Williams, P. Hwang, and S. Kitaigorodskii (1996). Estimates of kinetic energy dissipation under breaking waves. *J. Phys. Oceanogr. 26*, 792–807.

Thomson, J. (2012, 2013/01/03). Wave breaking dissipation observed with SWIFT drifters. *Journal of Atmospheric and Oceanic Technology 29*(12), 1866–1882.

Thomson, J., E. A. D'Asaro, M. Cronin, E. Rogers, R. Harcourt, and A. Schcerbina (2013). Waves and the equilibrium range at Ocean Weather Station P. *J. Geophys. Res. 118*, 1–12.

Thomson, J., B. Polagye, V. Durgesh., and M. C. Richmond (2012, July). Measurements of turbulence at two tidal energy sites in puget sound, wa. *J. Ocean. Eng Vol. 37*(3), 363–374.

Thornton, E. B. and R. T. Guza (1982). Energy saturation and phase speeds measured on a natural beach. *Journal of Geophysical Research 87*(C12), 9499–9508.

Thornton, E. B. and R. T. Guza (1983). Transformation of wave height distribution. *Journal of Geophysical Research 88*(C10), 5925–5938.

Wiles, P., T. P. Rippeth, J. Simpson, and P. Hendricks (2006). A novel technique for measuring the rate of turbulent dissipation in the marine environment. *Geophys. Res. Let. 33*, L21608.

Woodroffe, C. D. (2002). *Coasts: form, process, and evolution*. Cambridge Univ. Press.

Wright, L. D. and A. D. Short (1984). Morphodynamic variability of surf zones and beaches: a synthesis. *Marine Geology 56*, 93–118.

Appendix A

TURBULENT STRUCTURE FUNCTION SENSITIVITIES

Introduction

Structure functions are commonly used as a method to estimate turbulence in the ocean. While the structure function method often appears smoother than spectral methods, some studies claim the results are not as robust (Nichols-Pagel et al., 2008). Error estimates in dissipation rates from structure functions are difficult to quantify analytically. Additionally, doppler noise from velocity measurements can manifest as increased turbulence, and the effects of intermittence on the dissipation rate are not well quantified.

This appendix will attempt to evaluate how doppler errors and intermittence alter dissipation rates as they are measured by a SWIFT. First, the velocity measurements made onboard the SWIFT are discussed. Next, the effect of doppler measurement noise on the structure function is shown. Then, synthetic data with known structure is created, and 'sampled' as if it were measured with doppler noise. The resulting 'measured' dissipation rates are compared to the input dissipation rate which is known a priori. Lastly, intermittent time series are 'measured' and compared to the input dissipation rates.

Velocity Measurements

SWIFT velocity measurements are taken from an upward facing Nortek Aquadopp HR Acoustic Doppler Velocimeter, which measures water velocities accurate to $\pm 5\ mms^{-1}$ or to within 1% of the maximum velocity, whichever value is higher. The Aquadopp is mounted in the SWIFT hull such that the along beam distance to the surface is 80cm.

It is common to use the Reynolds decomposition where the total velocity is expressed as the sum of components due to mean currents, waves, and turbulence.

$$U = \bar{U} + \tilde{U} + u \tag{A.1}$$

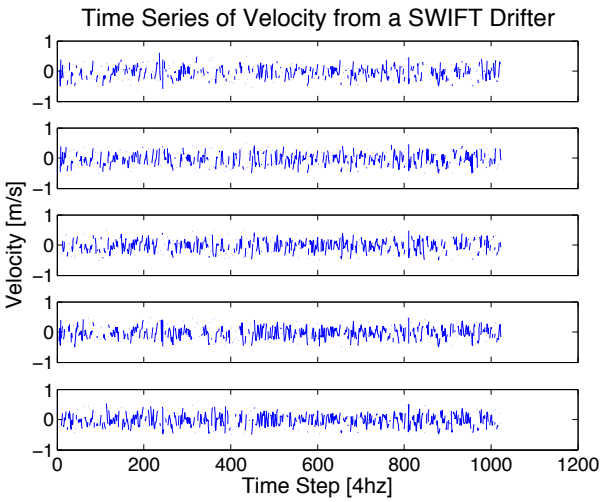

Figure A.1: Sample time series of the top five velocity bins as measured from the Nortek HR Aquadopp on board a SWIFT drifter. Only 5 of the 16 bins are shown because of space limitations. Missing values in the time series are due to quality control processing based on beam correlations and return intensity as described in Thomson et al. (2012). Data is processed in 5 minute bursts, the first 1024 samples are used for each 5 minute burst.

Where U is the total velocity, $\bar{U}$ is the mean velocity, $\tilde{U}$ is the wave orbital velocity, and u is the turbulent velocity component. The SWIFT follows mean currents as well as wave orbital velocities, such that the measured velocity is primarily the turbulent component, u, in the Reynolds decomposition. This helps avoid the 'phase wrapping' problem common with HR instruments, where velocities outside of the range $\pm 1\ ms^{-1}$ are ambiguous. An example velocity time series is shown in Figure A.1.

Structure Function

The SWIFT velocities are used to estimate dissipation rates (method described in §2.2) using the second order structure function, which is defined:

$$D(z,r) =< (u(z) - u(z+r))^2 > \tag{A.2}$$

Where z is the depth of the velocity measurement, r is the along beam lag distance between samples, u is the measured turbulent velocity, and the brackets represent a burst

average typically taken to be 5 minutes. Adding measurement noise $\sigma_{e,z}$ denoting the doppler measurement error at vertical location z yields:

$$D(z,r) =< (u(z) \pm \sigma_{e,z} - u(z+r) \pm \sigma_{e,z+r})^2 > \tag{A.3}$$

Taking the square gives:

$$\begin{aligned} D(z,r) =< & u(z)^2 + u(z+r)^2 - 2u(z)u(z+r) + 2u(z)\sigma_{e,z} + \\ & 2u(z+r)\sigma_{e,z} + 2u(z)\sigma_{e,z+r} + 2u(z+r)\sigma_{e,z+r} + 2\sigma_{e,z+r}\sigma_{e,z} + \sigma_{e,z+r}^2 + \sigma_{e,z}^2 > \end{aligned} \tag{A.4}$$

Assuming noise attributed to a velocity at depth z is independent from a velocity measurement at $z+r$, (i.e. $< \sigma_{e,z}\sigma_{e,z+r} >= 0$), and organizing covariance terms yields:

$$D(z,r) = \sigma_{U,z}^2 + \sigma_{U,z+r}^2 - 2\mathrm{Cov}\{u(z), u(z+r)\} + 2\mathrm{Cov}\{u(z), \sigma_{e,z}\} + 2\mathrm{Cov}\{u(z+r), \sigma_{e,z+r}\} + \sigma_{e,z+r}^2 + \sigma_{e,z}^2 \tag{A.5}$$

Commonly the measurement error terms $\sigma_{U,z}$ and $\sigma_{U,z+r}$ are treated as the same doppler noise error, independent of velocity measurements, such that $\mathrm{Cov}\{u, \sigma\} = 0$ and $\sigma_{e,z}^2 = \sigma_{e,z+r}^2$ (Thomson et al., 2012; Rusello and Cowen, 2011). The structure function can then be written:

$$D(z,r) = \sigma_{U,z}^2 + \sigma_{U,z+r}^2 - 2\mathrm{Cov}\{u(z), u(z+r)\} + 2\sigma_e^2 \tag{A.6}$$

In §2.2, it was shown that a noise intercept N results when fitting the structure function to $r^{\frac{2}{3}}$. Equation A.6 shows the intercept, N, is expected to relate to the doppler noise, $N = 2\sigma_2^2$. Intercepts, N, are therefore checked for the expected normal distribution in processing.

Modeling Turbulence from a White Noise Process

Studying the effect doppler noise on dissipation rates using in situ data is difficult, as the difference between noise and velocity in the measurement is ambiguous. Therefore, we will estimate structure functions through the following process. First, a time series of $u(z)$ with known turbulent quantities (i.e ϵ and TKE) will be generated by inverting the

structure function method described in §2.2. Next, the modeled velocity time series will be 'measured' by adding normally distributed noise to simulate doppler instrument noise σ_e. The synthetic time series will then be used in the second order structure function method to estimate dissipation rates. In this way we can compare the resulting synthetic turbulent quantities (i.e. ϵ_{meas} and TKE_{meas}) to the respective input values. Lastly, intermittence is studied by generating a step function time series of synthetic turbulence, sampling, and comparing the resulting turbulent quantities.

While the statistical model of turbulence offers more control over input variables ϵ and TKE, there will always be variability between the input and the synthetic quantities due to the nature of white noise processes. In addition, there is a floor to the degree of accuracy in which we can portray the error. In other words, if the added measurement error is less than the natural variability of the WN model, then it will be indistinguishable as added error. This downfall will be attempted to be circumnavigated by large sample sizes of Monte Carlo Simulations, but it will remain an issue if a greater degree of accuracy is required. For the purposes of evaluating patterns in the error in response to different noise and input stimulus, this approach is deemed to be sufficient.

In order to model turbulent velocities, an input of the total dissipative energy $\dot{E}$ is required. A dissipation rate per unit depth $\epsilon(z)$ profile can then be constructing by matching the total area under the $\epsilon(z)$ profile, or $\int \epsilon dz$ to the input dissipative energy $\dot{E}$ and assuming a logarithmic shape. An example of such a profile can be seen in Figure A.2.

Once a known $\epsilon(z)$ profile is created, the values of the second order structure function $D(z,r)$ for all relevant z and r can be equated to the time series variance and cross covariances, as shown in equation (A.6). An example plot showing the structure functions $r^{\frac{2}{3}}$ dependance can be seen in Figure (A.3). Since the goal of this section is to create a noise free velocity time series, the $2\sigma_e^2$ term in Equation A.6 will be set to zero. The following matrix shows an example set of equations for a three profile system (The profile order has been reduced for simplicity as typical measurement from a SWIFT include 16 depth bins).

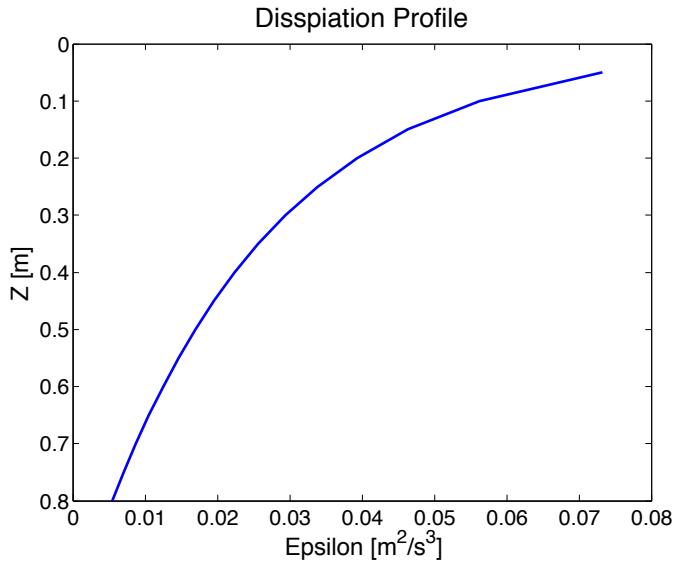

Figure A.2: Example dissipation profile created such that the area under the curve is equivalent to a given $\dot{E}$. The values presented here are larger than ones typically seen in situ.

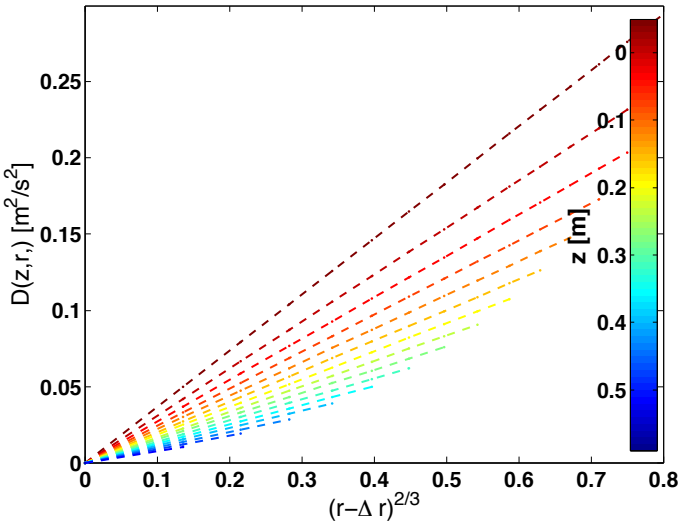

Figure A.3: Structure Function values calculated from an $r^{\frac{2}{3}}$ dependance

$$D(z,r) = \begin{bmatrix} 0 & \sigma_1^2 + \sigma_2^2 - 2\text{Cov}\{u_1, u_2\} & \sigma_1^2 + \sigma_3^2 - 2\text{Cov}\{u_1, u_3\} \\ 0 & 0 & \sigma_2^2 + \sigma_3^2 - 2\text{Cov}\{u_2, u_3\} \\ 0 & 0 & 0 \end{bmatrix} \tag{A.7}$$

The resulting set of equations is always underdefined (more unknowns than equations) by the number of velocity bins with depth, z. One solution is to specify the variance (i.e. TKE) for each time series (σ_1^2,σ_2^2... etc.) and solve for the covariance terms using Equation A.6. Since the system is always underdefined by the number of depth bins, this process will always yield the correct number of equations and unknowns to specify an exact solution. Arbitrary variances were used with a profile that loosely matches expected TKE profile shapes.

The Yule-Walker Method

A time series of velocity at depth, z, with a known covariance to depth $z + r$, can be constructed from a bottom up approach using a Yule-Walker moment matching scheme. Setting the bottom velocity bin to $WN(0, \sigma_1^2)$, the one-bin-up time series values (i.e. $u(z+r)$) are estimated using an AR(p) model (Auto-Regressive model of order p) using the previously estimated velocity bins as predictors. The order of the AR process is the number of the depth bin z. For example, the third bin from the lowest depth bin is expressed:

$$u(3,t) = \phi_1 u(2,t) + \phi_2 u(1,t) + Z_{3,t} \tag{A.8}$$

where $u(1,t)$ is the velocity of the first depth bin at time t, $u(2,t)$ is the velocity of second depth bin at time t, ϕ_1,ϕ_2 are the AR(p=2) coefficients, and Z is white noise variance. The ϕ coefficients are found using the Levinson-Durbin Recursions. The Levinson-Durbin Recursions take an input covariance sequence and solve for the AR coefficients. Here, the input covariance sequence is determined from the structure function. The variance of the WN process $Z_{z,t}$ in the AR(p) model is defined from the equation:

$$Z = \gamma(z) - \sum_{r=1}^{n-z} \phi_r \gamma(r) \tag{A.9}$$

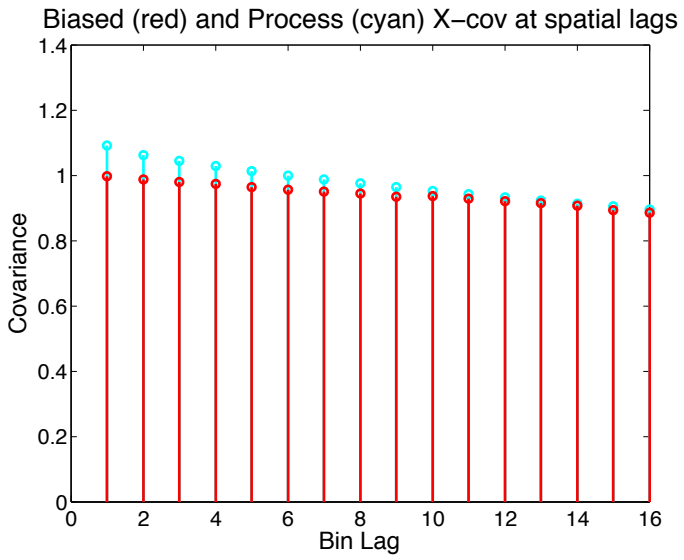

Figure A.4: Cross Covariance Sequence at zero time lag between spatial lags down from the bin nearest the surface

where $\gamma(z)$ is the variance of the time series at depth bin z, and $\gamma(r)$ is the covariance of the time series at spatial lag r. Examples of the model variance sequence with depth, and cross covariance sequence from the near surface bin can be seen in Figures A.5 and A.4 respectively.

Monte Carlo Simulations

The synthetic turbulent velocity data can be processed as is they were measured from a SWIFT to check that the input dissipations are modeled correctly. 10000 realizations of the WN model are shown in Figure A.6 along with the average profile with standard deviations. Variance in the synthetic profiles seems to increase near the surface. This is likely due to compounding errors; the synthetic data was created from the bottom up such that each velocity closer to the surface contains errors from all the velocities lower in depth. The mean profile of the 10000 realizations matches well with the input for the model.

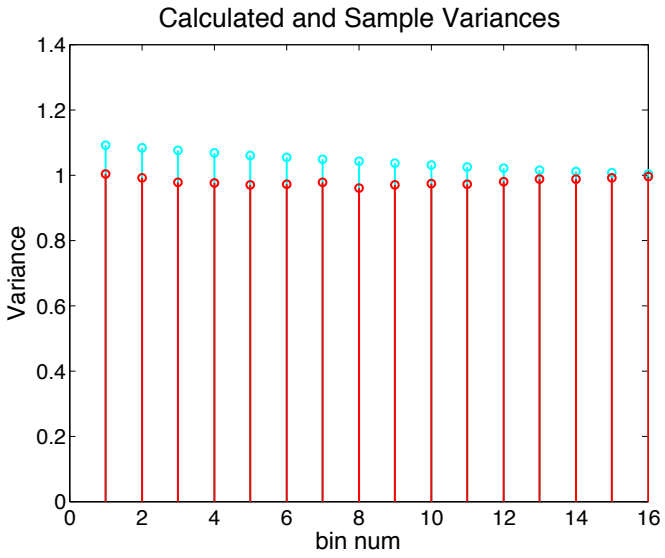

Figure A.5: Model and Given variance for each depth bin

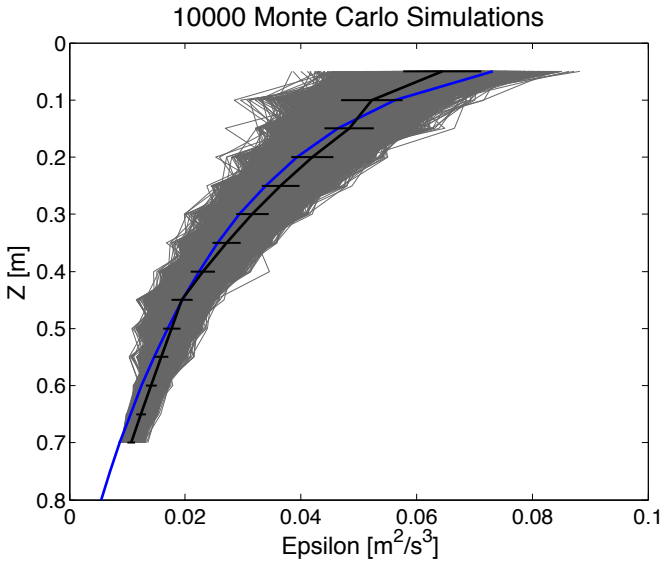

Figure A.6: 10000 Monte Carlo Simulations of dissipation profiles build from a WN model. Realizations are shown in grey, the average is shown with standard deviations in black, and the input profile is shown in blue.

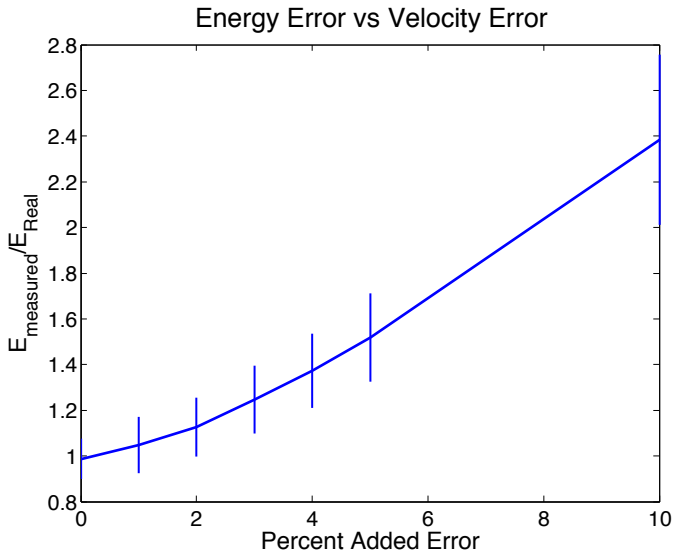

Figure A.7: Ratio of synthetic $\dot{E}$ to the prescribed $\dot{E}$ increases with added noise.

Error Estimation

Tests using the synthetic data can be done to evaluate the response of estimated dissipation rates to increasing measurement noise. The noise is added directly to the u(z) time series' created by the model before processing by the dissipation codes. The noise distribution is chosen to be normal in order to simulate doppler noise, and the variance of the process is determined as a percentage of the model time series' variance. A Monte Carlo simulation was run to evaluate the model response at each added noise percentage. The results are shown in Figure A.7. The synthetic dissipation rate increases relative to the prescribed dissipation rate when measurement noise is added.

Intermittence

Turbulent events are rarely constant for the duration of an averaging window. As a result, measured turbulent velocities time series are often non-stationary. Dissipation rates are often used to evaluate energy balances, which leads to the question: Does the energy loss implied by the average dissipation rate over the time series relate to the expected energy

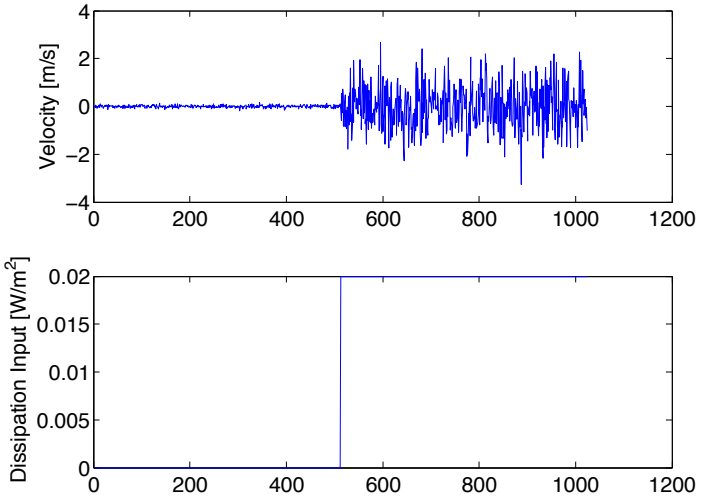

Figure A.8: A step-function type energy input (bottom) with a sample velocity profile (top).

loss from a non-stationary input? In a different form:

$$E_{meas} = t * \dot{E}_{meas} \stackrel{?}{=} \int_0^t \dot{E}_{Real} dt = E_{Real} \tag{A.10}$$

To answer this question, an intermittent time series is sampled (Figure A.8) and compared the the total input dissipation over the time series. The non stationary input is an extreme case where the background noise is approximately the instrument noise, and the event simulates sustained turbulence sustained under a large breaking wave. The relative energy output was evaluated for different event durations, again, using a Monte Carlo simulation for each case. The results are shown in Figure A.9.

Discussion

Doppler Noise

Figure A.7 clearly shows a relation between added measurement variance and measured dissipation rate estimates. This error is most likely due to one or both of two effects. The structure function will potentially treat non-uniform measurement variance in depth,z, as

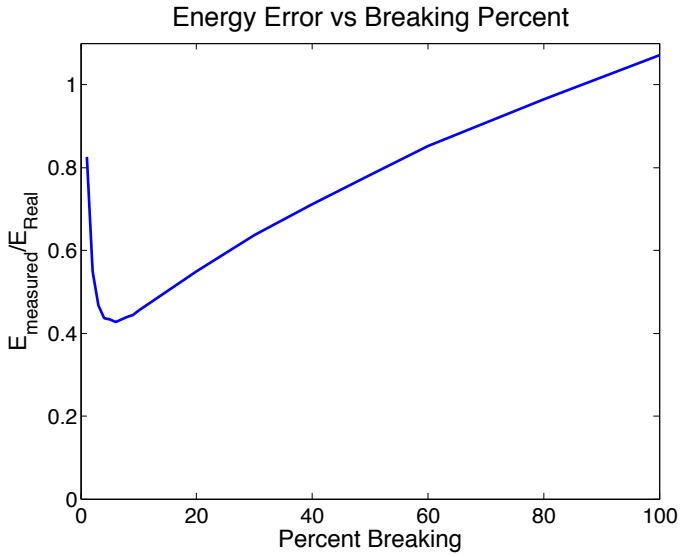

Figure A.9: Ratio of 'measured' E to the given E decreases with the duration of the turbulent event until the noise floor is reached at Percent Breaking $\approx 3\%$

turbulent velocity fluctuations (Equation (A.5). The second phenomena that could potentially cause large dissipation estimates is due to the linear fits between $D(z,r)$ and $r^{\frac{2}{3}}$ (§2.2). At the deepest velocity bins, the number of lags available decreases, and therefore there are fewer points to determine the slope between $D(z,r)$ and $r^{\frac{2}{3}}$. Fits with fewer points are susceptible to errors in slope estimates, and because the structure function is always positive, these slope variances bias high with more variation in the structure function. This phenomena is seen in profiles with high measurement noise, manifesting as large $\epsilon(z)$ values lower in the water column, though dissipation rates are expected to be largest at the surface. Under the normal operating parameters of the HR Aquadopp used on board the SWIFT (variance $\leq 1\%$), this source of error is not expected (Figure A.7). Regardless, this result implies precise measurement of velocities are needed to estimate turbulent dissipation rates, with doppler noise σ_e^2 on the order of less than 2% of the TKE (i.e. measured variance).

Intermittence

Based on the results above, it was expected for energy estimates to be higher than the input energy in an intermittent time series, as the doppler noise results in a non-zero synthetic dissipation rate when no turbulence is sampled. This effect is seen to a small degree in Figure A.9 when the signal to noise ratio is low for low percent breaking rates. Above this noise floor, the measured energy is always lower than the real energy. This intriguing result is most likely attributed to an averaging effect in converting from dissipation rates ($\dot{E}$) to an energy lost E. It should be noted that the event in this time series is notably large for the background signal compared to what might be seen in situ. As a result this effect might be magnified.

Conclusion

A statistical model of turbulent velocities is constructed based on a $r^{\frac{2}{3}}$ relationship with the second order structure function. Monte Carlo simulations are used to evaluate the effect of measurement noise on dissipation estimates. A positive increasing relationship is found between ratio of measured dissipated energy to synthetic dissipated energy with respect to increasing doppler measurement error. A second test is done to evaluate the measurement response to an intermittent input signal. The result is also surprising, as the measured energy is always less than the input energy, seemingly in contrast to the first result. Measurements errors from the HR Aquadopp on board the SWIFT drifter are expected to have a negligible effect on the total measured dissipative energy, but it should be noted that the error can increase significantly if the doppler noise increases. Careful quality control measures are therefore suggested when evaluating turbulence data using a second order structure function method.

Appendix B

RAY TRACING

While a 1-D Wave energy flux equation is often assumed, refraction of waves over varying bathymetry can converge or diverge wave rays focusing or diffusing wave energy. Wave refraction is a manifestation of the dispersion relation. Waves travel slower in shallow water, thus a single wave crest which extends over varying depths will curve as the crest segment in deep water out runs the shallow crest segment. This is analogous to the outside wheels on a turning car spinning faster than the inside wheels.

Estimating wave ray paths can be done through definition of the the phase function, Ω:

$$\vec{k} = \nabla\Omega \tag{B.1}$$

and

$$\omega = -\frac{\partial\Omega}{\partial t} \tag{B.2}$$

The general form governing wave ray tracing is known as Snell's law is then:

$$\nabla \times \vec{k} = 0 \tag{B.3}$$

The quantity must be zero because the cross product of a gradient is zero. For straight bathymetry refraction Snell's Law reduces to:

$$\frac{\sin(\alpha_0)}{C_0} = \frac{\sin(\alpha)}{C} \tag{B.4}$$

Where α is the wave ray direction, C is the phase speed, and the subscript $_0$ designates the offshore condition. This form is most similar to the Snell's law used for optics.

The effect of heads, or outward protrusions in the coastline, focus wave rays, while embayments do the opposite. Figure B.1 shows a cartoon demonstrating this effect. Area's of

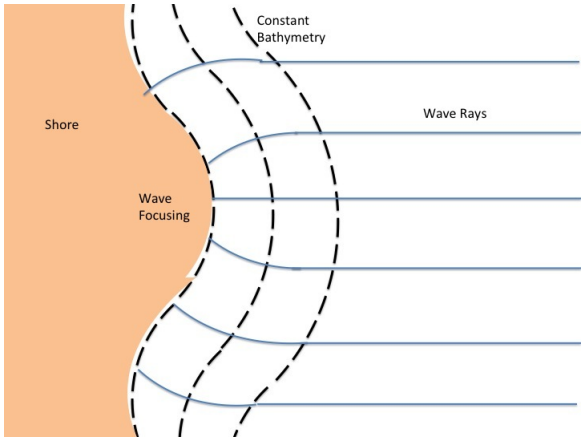

Figure B.1: Wave Rays bend toward lines of constant bathymetry. Headlands focus wave rays as seen above.

wave focusing increase in 1-D wave energy flux (energy flux is conserved two dimensionally) as energy is compressed in the alongshore direction.

Because the simplified Equation B.4 is not valid over complex bathymetry, a more in-depth analysis of wave rays is needed. By definition, the curvature of the wave ray is due to the gradient in wave speed along the wave crest. One ray tracing technique estimates the phase speed of the wave everywhere given wave period and bathymetry, and then steps wave rays forward from an initial position. This method is used to calculate wave ray paths at New River Inlet in Figures B.2, B.3 and B.4 for periods of 5, 7, and 10s respectively.

Figures B.2, B.3 and B.4 show that refraction is relatively small until cross shore coordinate $x = 400$m. Waves are focused over the shoal between the two channels, and over the shoal near North Topsail Island. Figure B.2 shows a wave ray at $T = 5$s refracting almost 90° from the other wave rays over the North Topsail shoal. This is consistent with visual observations of the shoal, where waves were often seen traveling at large angles relative to the incoming swell.

These Figures also exemplify a shortcoming of the radiative transfer equation. When wave rays cross (known as a caustic) the wave energy flux becomes infinite. Figures B.2, B.3 and B.4 show rays crossing at many locations around the inlet at each of the three wave

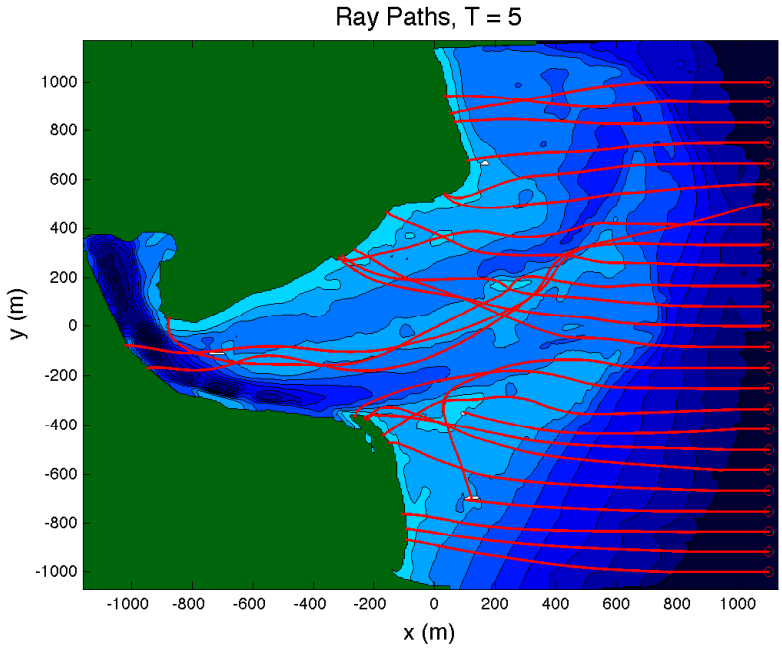

Figure B.2: Wave Rays bending over bathymetry with an offshore period of 5 seconds.

periods.

Currents, in addition to bathymetry, can refract waves. A gradient in current will change the wave speed along a crest (similar to depth effects), curving the wave. When currents oppose waves, the effect turns waves to face the currents. This can trap waves in a current jet called a wave guide, as seen in Figure B.5. The opposite is true for following currents, as the additive effect of currents increase the wave phase speed such that it outruns the rest of the wave crest. This can create a caustic as wave rays cross when they refract away from the jet of following current. For a uniform current across a wave crest, no refraction occurs as there is no gradient in phase speed across the wave crest.

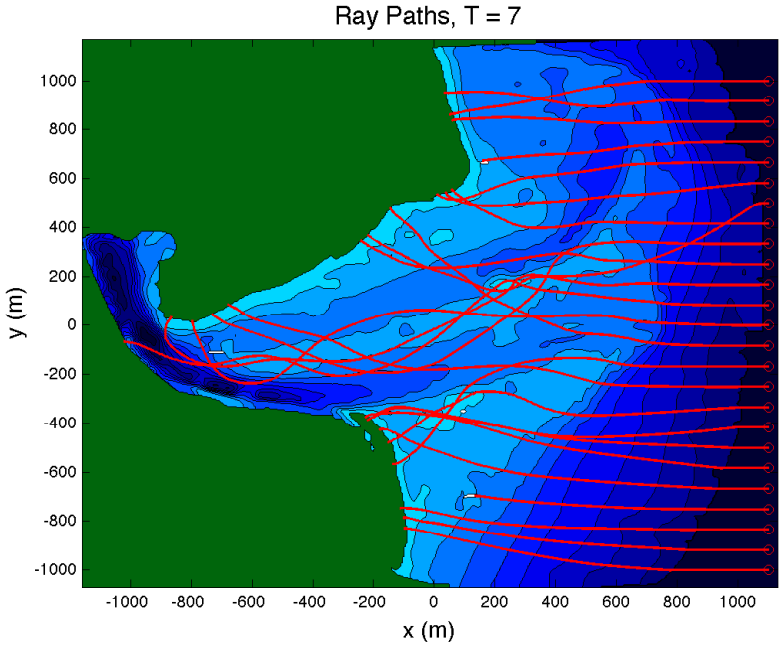

Figure B.3: Wave Rays bending over bathymetry with an offshore period of 7 seconds.

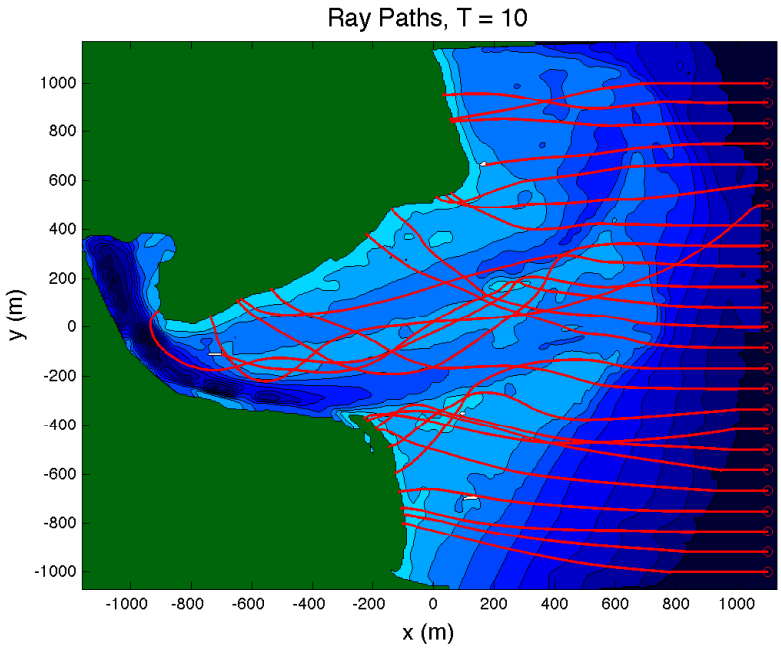

Figure B.4: Wave Rays bending over bathymetry with an offshore period of 10 seconds.

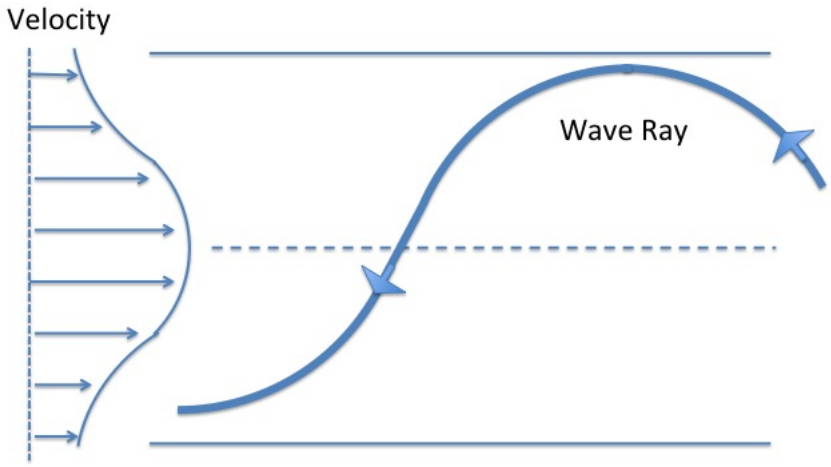

Figure B.5: Wave rays refract due to a gradient in currents. When currents oppose the wave directions, the wave rays bend to face the currents. Some wave rays are trapped in the opposing jet.